

LIBRARY Michigan State University

This is to certify that the

dissertation entitled

Spin Accumulation and Detection in Non-Magnetic Metals Using Singh Domain Ferromagnetic Metal Nanoparticles

presented by

CHARLES EDWARD MOREAU

has been accepted towards fulfillment of the requirements for

Ph.D. degree in Physics

Major professor N. Birge

Date 08/10/01

MSU is an Affirmative Action/Equal Opportunity Institution

0-12771

PLACE IN RETURN BOX to remove this checkout from your record.

TO AVOID FINES return on or before date due.

MAY BE RECALLED with earlier due date if requested.

DATE DUE	DATE DUE	DATE DUE
	<u> </u>	

6/01 c:/CIRC/DateDue.p65-p.15

SPIN ACCUMULATION AND DETECTION IN NON-MAGNETIC METALS USING FERROMAGNETIC METAL NANOPARTICLES

By

Charles Edward Moreau

AN ABSTRACT OF A DISSERTATION

Submitted to
Michigan State University
in partial fulfillment of the requirements
for the degree of

DOCTOR OF PHILOSOPHY

Department of Physics and Astronomy

2001

Norman O. Birge

ABSTRACT

SPIN ACCUMULATION AND DETECTION IN NON-MAGNETIC METALS USING FERROMAGNETIC METAL NANOPARTICLES

By

Charles E. Moreau

Linear arrays of 15nm thick, polycrystalline $Co_{91}Fe_{9}$ nanoelements have been fabricated using e-beam lithography, collimated sputtering and lift-off. The elements have widths of 0.17 and 0.25 μ m, lengths from 0.5 to 4 μ m, pointed ends, and center-to-center spacing of 0.5 μ m. Characterization by magnetic force microscopy shows that in the virgin state these elements are single-domain and have magnetizations parallel to their long axes. The field at which an element switches its magnetization direction is shown to depend mainly on its width, and only slightly on its length. Fields of about 440 and 680Oe are needed to switch completely the 0.25 and 0.17 μ m structures, respectively. This separation in switching fields is adequate to allow elements of different widths to be switched independently. Also, magnetic force microscopy and super-conducting quantum interference magnetometry analysis show that a capping layer is necessary to protect the films from oxidation. Unprotected films show an altered hysteresis loop and their associated nanostructures are not consistently single-domain.

Using these nanoelements, we have measured the magnetoresistance (MR) of hybrid ferromagnetic/normal (F/N) structures fabricated with a planar geometry, using multi-level electron beam lithography. The samples consist of two single-domain nanofingers crossed by a 200nm wide Ag wire. The F elements have lengths of 2μ m, widths of 250 and 175 μ m respectively, and are placed parallel to each other with a center-to-center spacing of 400μ m. The different widths enable us to change the magnetization direction of the fingers independently. When we apply the current

between two F elements via the N wire, the device is somewhat analogous to a traditional F/N/F perpendicular current (CPP) spin valve sandwich. Magneto-transport measurements on our sample show the typical spin valve effect. Though the effect is relatively small for these devices ($\frac{\Delta R}{R} = 4 \times 10^{-4}$), it is commensurate with theoretical predictions.

There are several experiments we plan to perform in the near future using this new approach to spin polarized transport. These include using multiple F elements to see the dependence of the spin-dependent signal on the distance between the spin injector and detector, as well as an experiment where the current leaves via the normal wire.

ACKNOWLEDGEMENTS

During my time as a graduate student I've found that the assumption of people in the greater world outside of academia is that graduate students eventually graduate. Unfortunately, there are far to many ways not to finish a degree. Without support from professional and personal sources, it would be all but impossible to accomplish such an arduous task. As such, I would like to acknowledge the assistance of those without whom this dissertation would not have been possible.

To begin I would like to thank my advisor, Norman Birge, for his time and patience during my time at MSU. From him I have learned not just subject matter, but how to function as a professional.

Second, it is imperative to give Juan Caballero proper credit for his role in this work. During his post-doctoral work here at MSU, Juan worked closely with this project and helped develop the rather involved fabrication processes used in this work, as well as the design of the device. His efforts during the boot-strap phase of this project were vital to its success.

Next I wish to thank Professors Jack Bass and William P. Pratt, Jr. for their role as valuable resources of knowledge, and for providing substantial laboratory support for this work, including the use of the sputtering system and the quick dippers.

The technical staff employed by the department have also been indispensable to this work. There is Baokang Bi, who manages the Keck Microfabrication facility, and who has provided constant education in lithographic fabrication techniques as well as microscopy. Also, there is Reza Loloee, who manages the sputtering system in particular, who has assisted me in the deposition and processing of the magnetic materials. In addition to their prescribed jobs, both have lent to me their personal and professional knowledge and expertise in many areas of science.

This work was supported by the National Science Foundation Center for Sensor

Materials (DMR-9809688), the Ford Research Laboratories, the Keck Microfabrication Facility, and NSF Grant (DMR-9801841)

There must be mention of my fellow graduate students for playing their role in this communal endeavor: David Hoadley, Matthew Miller, Barton Pritzl, Remo DiFranceso, Robert Slater, Peter Peterson, Michael Davis, Ryan Kruse, Aaron La-Cluyze, and Randy Yarger. I thank you all, and apologize for leaving anyone out.

Finally I would like to thank my family for their love and patience: my wife Caryn, and my children, Riley and Elayna. They have accepted a husband and father distracted by the toils of graduate school. I am greatly excited to return my full attention to them. To my parents I send thanks for emphasizing the importance of education.

Table of Contents

LIST OF TABLES viii				
LI	ST (OF FIGURES	ix	
1	Inti	roduction	1	
	1.1	Short Introduction to Magnetism	2	
		1.1.1 Electron Spin and Magnetic Moment	2	
		1.1.2 Magnetic Dipole Interaction	3	
		1.1.3 Ferromagnetism	4	
		1.1.4 The Spin Wavefunction	5	
		1.1.5 Heisenberg Ferromagnetism	6	
	1.2	Magnetism in Technology	7	
		1.2.1 Hard Disk Drive Media	8	
		1.2.2 Hard Disk Drive Read Heads	9	
		1.2.3 Magnetic Random Access Memory	10	
	1.3	Motivation for This Work	10	
2	Swi	tching in Magnetic Structures: Background and Theory	13	
	2.1	Domain Structure	13	
	2.2	Magnetization Direction	14	
		2.2.1 Magnetocrystalline Anisotropy	14	
		2.2.2 Strain Anisotropy	15	
		2.2.3 Shape Anisotropy	16	
		2.2.4 Comparison of Anisotropy Energies	18	
		2.2.5 Acicular Nanoelements	19	
		2.2.6 Meaning of Demagnetizing Factors	19	
	2.3	The Switching Field	22	
3	Swi	tching in Magnetic Structures: Experimental Procedure	27	
	3.1	Electron Beam Lithography	27	
		3.1.1 Specific Notes Regarding Electron Beam Lithography	28	
	3.2	Collimated Sputtering	30	
	3.3	Magnetic Force Microscopy	32	
		3.3.1 Limitations of Magnetic Force Microscopy	34	
		3.3.2 Specific Notes Regarding Magnetic Force Microscopy	38	
	3.4	Sample Preparation and Measurement	38	
4	Swi	tching in Magnetic Structures: Experimental Results	41	
	4.1	Fabrication of Single Domain Elements	41	
		4.1.1 Co ₉₁ Fe ₉ Thin Films	41	
		4.1.2 Co ₉₁ Fe ₉ Nanostructures	43	

	4.2	Controlling the Switching Field	48		
5	Spir	Spin-Polarized Transport: Background and Theory			
	5.1	GMR Quickly	56		
	5.2	Two-Current Series-Resister Model	58		
		5.2.1 Parallel Magnetizations	60		
		5.2.2 Antiparallel Magnetizations	61		
		5.2.3 Calculating the GMR Signal	61		
	5.3	Application of ΔR	63		
6	Spir	n-Polarized Transport: Experimental Procedure	65		
	6.1	Multi-level Lithography	65		
		6.1.1 Photolithography	65		
		6.1.2 Alignment	68		
	6.2	Ion Milling	70		
	6.3	The Quick Dipper	70		
	6.4	Sample Mounting	71		
	6.5	Low Noise Measurement Circuit and Techniques	74		
7	Spir	n-Polarized Transport: Experimental Results	77		
8	Con	aclusions	85		
LI	ST (OF REFERENCES	89		

List of Tables

1.1	Symmetrized Spin Wavefunctions	6
2.1	Magnetocrystalline Anisotropy Constants, K ₁	15
2.2	Magnetization Energy Densities	18
2.3	Demagnetizing Factors for Limiting Cases	22
3.1	Electron Beam Lithography Recipe	27
3.2	JOEL EBL Parameters	28
4.1	Comparison of Stoner-Wohlfarth Prediction to Switching Results	51
6.1	Photolithography Recipe	66
6.2	Step-by-step EBL Alignment	69
6.3	Ion Milling Parameters	70
7.1	Run Parameters for Additive Sample	79
7.2	Run Parameters for Subtractive Sample	81

List of Figures

2.12.22.3	Origin of the Demagnetizing Field
3.1 3.2	Generalized EBL Process
3.3	Collimating Body
3.4	AFM Tip
3.5	AFM Tip Closer
3.6	AFM Tip Closer Still
3.7	MFM Cartoon
3.8	MFM Example, Single-domain
3.9	MFM Example, Multi-domain
3.10	Solenoid
4.1	Co ₉₁ Fe ₉ Thin Film SQUID
4.2	$Co_{91}Fe_{9}$ Thin Films With Al Protection
4.3	$Co_{91}Fe_{9}$ Collimated Thin Films
4.4	MFM of Co ₉₁ Fe ₉ Fingers
4.5	MFM of Co ₉₁ Fe ₉ fingers
4.6	Switching of Fingers
4.7	Determining the Switching Field
4.8	Results of switching experiment
4.9	Results of switching experiment
1.0	
5.1	GMR Cartoon, Parallel Alignment
5.2	GMR Cartoon, Antiparallel Alignment
5.3	Schematic Representation of a Planar Device
6.1	Overview of Photomask
6.2	
6.3	Schematic of Quick Dipper
6.4	Sample Measurement Circuit
7.1	SEM Image of a Planar GMR Sample
7.2	GMR Signal From Additively Patterned Sample
7.3	GMR Signal From a subtractively Patterned Sample
8.1	Improved Sample Design

Chapter 1: Introduction

Magnetism and magnetic substances have been known to man since ancient times. There are written accounts that date the knowledge of magnetism in lodestone (magnetite) to at least 600B.C., and it is possible that the Chinese used a compass as early as 2500B.C.[1] This early knowledge of magnetism can be attributed to the existence of permanent magnets. Permanent magnets are materials which posses a spontaneous magnetization, even at elevated temperatures. It must have seemed quite extraordinary four thousand years ago to find a rock that would attract objects through an invisible force. Since those ancient times, permanent magnets and electromagnets have been used in myriad devices and technological applications. From compass needles to cars, magnets are everywhere. Magnetic fields, both from permanent magnets or generated by electricity, also have been employed in everything from the medical profession to mall security. It is no small wonder, then, that there should be a strong interest in investigating the fundamental properties of magnetism.

But there is more than just credit cards and cellular phones to spur our efforts. Magnetism as an intellectual pursuit has great intrinsic interest. Magnetism represents a complex many-body ground state for electrons which, unlike another such ground-state, the superconducting state, persists at high temperature. Moreover, like superconductivity, magnetism is a purely quantum mechanical effect. This fact is masked by the many historical explanations of magnetism, all of which, as we shall see shortly eventually lead down the same blind alley: classically there is no ferromagnetism. But even in the light of quantum mechanics, magnetism, like many problems that involve electrons in materials, proves to be a difficult problem, with many unanswered questions.

1.1 Short Introduction to Magnetism

So the real root of magnetism, like superconductivity, is the motion and spin of the electron. The ground state of a BCS superconductor is made up of quasi-particles that look like paired electrons[2]. The constituents of such a pair have oppositely directed momenta and spins. In the case of magnetism, we have a ground state that is described by electrons with net orbital and spin angular momenta. For the purposes of this dissertation we will be primarily concerned with the latter.

1.1.1 Electron Spin and Magnetic Moment

The spin angular momentum of the electron was first devised to explain the magnetic field induced splitting in atomic spectral lines that were observed by Zeeman in 1896[3]. He suggested that an electron has a magnetic moment, $\vec{\mu}$, which is the result of its intrinsic spin angular momentum. With the advent of relativistic quantum mechanics, this spin was found to be an inherent property of the electron. This spin may be completely described by two quantities: S, the total moment of the particle, and S_z , the projection of the total moment onto the z-axis. Why the z-axis? Well, it need not be the z axis. In need only be an axis. Once the projection of the spin is measured on one axis, then there is no information to be had about projections onto the other two axes. The reason comes for the fact that in the quantum mechanics formalism, the spin operators \hat{S}_x , \hat{S}_y , and \hat{S}_z all commute with the total spin-angular momentum operator, \hat{S}^2 , but not with one another. This implies that there is a Heisenberg uncertainty relation between values of the spin along axis. By knowing one, we can forget about the others.

So, the magnetic moment of the electron can be written as follows[3]:

$$\vec{\mu} = -g \frac{e}{2m_e c} \langle \hat{S}_z \rangle \hat{z}. \tag{1.1}$$

Here, e is the charge of the electron, m_e is the mass of the electron, c is the speed of light in vacuum, and \hat{z} is the unit vector along the z-axis. For the electron, g has a value of close to 2. \hat{S}_z for the electron, which is a spin- $\frac{1}{2}$ particle, may have values of

$$\langle \hat{S}_z \rangle = \pm \frac{1}{2} \hbar. \tag{1.2}$$

Substituting Equation 1.2 into Equation 1.1 gives

$$\vec{\mu} = \mp g \frac{e\hbar}{2m_e c} \tag{1.3}$$

or

$$\vec{\mu} = \mp g\mu_B \hat{z} \tag{1.4}$$

where we have introduced the Bohr magneton μ_B .

1.1.2 Magnetic Dipole Interaction

In the subsequent discussion of magnetism, electrons will be treated as simply magnetic dipoles whose moment is given by 1.4. A collection of moments that spontaneously aligns is said to be ferromagnetic. But what causes the alignment? The first logical place to begin looking is the dipolar magnetic interaction. The magnetic field of a dipole is

$$\vec{B}(\vec{x}) = \frac{3\hat{n}(\hat{n} \cdot \vec{\mu}) - \vec{\mu}}{|\vec{x}|^3} \tag{1.5}$$

where \vec{x} is the vector between the dipole and the field point and \hat{n} is the unit vector in the direction of \vec{x} . Here I have deliberately omitted the delta function term from Equation 1.5[4]. When a second dipole is brought from infinity to a point \vec{x} we may

calculate the energy from

$$E = -\vec{\mu} \cdot \vec{B}(\vec{x}). \tag{1.6}$$

Substituting equation 1.5 for moment 1 into Equation 1.6 for moment 2, we have

$$E = -\frac{3(\vec{\mu}_2 \cdot \hat{n})(\hat{n} \cdot \vec{\mu}_1) + \vec{\mu}_2 \cdot \vec{\mu}_1}{|\vec{x}|^3}.$$
 (1.7)

Neglecting the angular dependence of Equation 1.7, and substituting into it Equation 1.3, we have

$$E \approx \frac{(g\mu_B)^2}{x^3} \approx (\frac{e^2}{\hbar c})^2 (\frac{a_0}{r})^3 \frac{e^2}{a_0} \approx \frac{1}{(137)^2} (\frac{a_0}{r})^3 Ry[5]$$
 (1.8)

where a_0 is the Bohr radius equal to $\frac{\hbar^2}{m_e e^2} = 0.529 \times 10^{-8} \text{cm}$, and Ry is the Rydberg constant equal to 13.6eV. Using for the distance between spins, r, something on the order of 2Å, then Equation 1.8 gives a value of about 10^{-4}eV .

Comparing the above energy to thermal energy at room temperature (300 K), $\sim 10^{-2} \text{eV}$, and the energy of the electrostatic (coulomb) interaction (fractions of an eV) reveals that the magnetic dipole interaction cannot by itself explain ferromagnetism. We must therefore seek out another explanation.

1.1.3 Ferromagnetism

It is apparent that lacking a classical argument for ferromagnetism, we will require a quantum mechanical approach. The explanation for ferromagnetism, in fact, comes about by way of symmetrizing the wave function for a many-electron system. The discussion of this section follows from *Ashcroft & Mermin* [5]. In the process of searching for a many-body ground state wave function for a collection of

electrons, we look for clues in the Hamiltonian of the form for two electrons

$$\hat{H} = -\frac{\hbar^2}{2m} (\nabla_1^2 + \nabla_2^2) + \frac{e^2}{|\vec{r}_1 - \vec{r}_2|}$$
 (1.9)

The last term in Equation 1.9 represents the coulomb potential. This potential is symmetric under exchange of the two particles. Therefore eigenstates of the Hamiltonian will possess definite exchange symmetry. The Pauli exclusion principle dictates that for electrons the total wave function is antisymmetric under exchange of the particles. Next we notice that the Hamiltonian is independent of spin. This allows us to separate the total wavefunction into a product of a spatial wavefunction and a spin wavefunction:

$$\Psi = \Psi_{spatial} \Psi_{spin}. \tag{1.10}$$

1.1.4 The Spin Wavefunction

We begin by looking for the properly symmetrized wave functions, Ψ_{spin} . Using the vector formalism we may write for a two spin system a state

$$|\Psi_{spin}\rangle = |Sz, 1, Sz, 2\rangle = |\uparrow, \uparrow\rangle, |\uparrow, \downarrow\rangle, |\downarrow, \uparrow\rangle, |\downarrow, \downarrow\rangle$$
(1.11)

Where an up arrow indicates a spin up electron and a down arrow represents a spin down electron. These states form a complete set of simultaneous eigenstates of \hat{S}^2 and $\hat{S}^{z,1}$, $\hat{S}^{z,2}$. Therefore, any linear combination of these states will also be eigenstates. We build properly symmetrized wavefunctions out of the vectors in Equation 1.11 by requiring that they be eigenstates of the exchange operator $\hat{P}_{1,2}$, such that

$$\hat{P}_{1,2}|S_{z,1}, S_{z,2}\rangle = \pm |S_{z,2}, S_{z,1}\rangle \tag{1.12}$$

The properly symmetrized (and normalized) wavefunctions are listed in Table 1.1 along with their various eigenvalues. The first wavefunction in Table 1.1 is

State	S	S_z	$P_{1,2}$
$\frac{1}{\sqrt{2}}(\uparrow,\downarrow\rangle - \downarrow,\uparrow\rangle)$	0	0	-1
$ \uparrow,\uparrow\rangle$	1	1	1
$\frac{1}{\sqrt{2}}(\uparrow,\downarrow\rangle+ \downarrow,\uparrow\rangle)$	1	0	1
$ \downarrow,\downarrow\rangle$	1	-1	1

Table 1.1: The properly symmetrized spin wavefunctions for a two particle system. The first wavefunction, with spin=0 is antisymmetric under exchange of the particles, while the next three, with spin=1, are symmetric under exchange of the particles.

antisymmetric under exchange of the particles. This is termed the singlet state, and is nonmagnetic as it has total spin equal to zero. The next three are all symmetric under exchange, and are called the triplet states. These are the magnetic states, as they have total spin equal to 1.

If the total wavefunction is to be antisymmetric, we must build products like Equation 1.10 using spatial and spin wavefunctions of opposite symmetry. What is required for ferromagnetism is to have the triplet state (spin=1) preferred over the singlet state (spin=0). Such a triplet state would have an anti-symmetric spatial wave function. Since the Hamiltonian is independent of spin, it is sufficient to show that the anti-symmetric spatial wavefunction has lower total energy than the symmetric.

1.1.5 Heisenberg Ferromagnetism

The argument that we've been pursuing follows from that of Heisenberg in 1928. [6, 7, 8, 9]. This was the first method that put ferromagnetism on a quantum mechanical footing. The argument addresses the last point in Section 1.1.4 by pointing out that the symmetric eigenstates of the spatial Hamiltonian will have greater probability density of having $r_1 = r_2$ than do the antisymmetric eigenstates. Since the potential energy of the problem is the coulomb interaction which goes as

the inverse of distance, the symmetric states might be expected to have higher energy than the antisymmetric. Thus we may write for the ground state of the problem a wavefunction that consists of an antisymmetric spatial wavefunction multiplied by a symmetric (spin=1) spin wavefunction, as we wished to.

Well, just about as soon as the argument was formulated, it was realized that there were problems with it. For instance, the ground state of the hydrogen molecule (H_2) is in fact a spin singlet, not a triplet. In fact, for the case of two electrons just presented, it was shown that there is a fundamental theorem that dictates just the opposite energy ordering, and thus the antiferromagnetic state is preferred[5]. The proper formalism to prove the energy ordering for N electrons is, it turns out, significantly more involved, and must be applied on a material by material basis. In fact, there are a great many more antiferromagnetic materials than ferromagnetic. The shortcoming in the Heisenberg formalism is that it only takes into account first order perturbative corrections to the Hamiltonian. The second order corrections, it turns out, aren't negligible in general, and must be calculated for each material. However, Heisenberg's exchange approach, while not complete, did show a path to a quantum mechanical description of ferromagnetism.

1.2 Magnetism in Technology

Magnetic materials certainly have played a vital role in all sorts of technologies. However given the commercial importance of computer technology it is appropriate to give some attention to how magnetic materials have and will continue to drive technological innovations. Novel devices that employ magnets or the spin properties of electrons are still being developed to expand upon current technology, or develop new ones[10]. To illustrate this, consider three areas where the properties of magnetic materials play a crucial role in current technology: hard disk read heads,

hard disk media, and magnetic random access memory (MRAM).

1.2.1 Hard Disk Drive Media

Current Hard disk drives utilize platters coated with a magnetic thin film, typically CoCrPtTaB or CoCrPtTaNb[11]. Thin film technology suffers from a fundamental bit density limit, which occurs when there is enough thermal energy available to overcome the energy barrier to switching. In thin film recording, the number of crystallographic grains that constitute a bit must remain constant in order to maintain an adequate signal-to-noise ratio. In order to shrink the bit, then, one must shrink the grain size. However, as the grain size shrinks, so too does the energy required to flip them [12]. Thus as the density of the bits increases, and hence the size of each bit decreases, so to does the energy barrier to switching. At some critical size, the amount of thermal switching of bits becomes unacceptable, and the information stored in the device is lost. This limit, known as the superparamagnetic limit[13, 14, 15, 16] was estimated to occur at $40\frac{Gbit}{in^2}$ [17]. To date, there are two strategies for clearing this hurdle. The first continues using thin film media, but substitues for the single metal layer a pair of layers sandwiched around an extremely thin (≈ 6 Å) layer of ruthenium[18, 19]. The result is that bits consist of two antiferromagnetically coupled domains, one above the other and separated by the ruthenium. Such media has been appropriately named antiferromagnetically coupled (AFC) media. This technique is expected to reach $100\frac{Gbit}{in^2}$. In addition to this advanced thin film technology, there is a push to develop perpendicular recording or patterned recording media. Here, the bits are comprised of, say, columnar magnetic structures whose magnetization lies normal to the platter surface, or single-domain nanometer size structures whose magnetization lies in the plane of the structure. The uncompensated poles at the ends of such structures represent the bits to be written and read. Here the density limit is a function of the density of packing such structures on a planar surface, barring any interaction effects [20, 21]. Methodologies have been suggested for producing such discrete media with densities of up to $50\frac{Gbit}{in^2}$ [22, 23, 24].

1.2.2 Hard Disk Drive Read Heads

Hard disk read heads have also benefitted from magnetism research. Historically, read heads were simple inductive devices which read and wrote data via a coil wrapped around a magnetic pole piece. These were replaced in the early 1990's by a design that relied on the anisotropic magnetoresistance (AMR) of the head. The AMR of a magnetic material depends on the angle between the electrical current and the internal magnetization of the read head, the latter being a function of the external magnetic field from the bits. These head designs were more sensitive, and hence could be made smaller than the previous inductive designs. However as the bit density of the hard drive platters increased, the volume of magnetic material and also the spatial extent of each bit decreased. So, in 1997 [12] IBM developed the first giant magnetoresistance (GMR) read head. GMR, like MR, is a field dependent resistance. In the case of GMR the value of the resistance is a function of the angle between the magnetizations of two ferromagnetic thin films which are separated by a thin spacer. These devices are often termed spin valves, and are typical of a general class of devices which consist of four layers. There is the free magnetic layer, which switches with the applied magnetic field, the spacer, the pinned magnetic layer, and the pinning layer which is an antiferromagnet that couples strongly to the pinned layer, preventing it from switching freely in the external applied field. The development of the GMR heads allowed for even smaller bits and higher bit densities.

1.2.3 Magnetic Random Access Memory

Historically, ferromagnetic structures were used as memory elements as early as the late 1940's[25]. These designs, though consuming little power, were quite slow when reading and writing. So the computer industry developed random access memory (RAM) designs that used capacitors (DRAM) and transistors (SRAM) as the bit elements. These proved much faster, and could be made more dense, than the ferromagnetic alternative. However, these newer types of memory required much greater power (capacitors must be refreshed due to voltage leaks, transistors sink current either in the on or off state), and are volatile, which means when the power is removed from the device, all information is lost. Ironically, both of these problems could be resolved by returning to magnetic elements. Improvements in fabrication techniques now make it possible to produce dense arrays of magnetic elements which can be addressed individually, and serve as RAM. This magnetic random access memory (MRAM) would offer the features of low power consumption, non-volatility, and fast switching speeds[26, 27, 28, 29]. Most of these designs involve a tunnelling GMR effect using multi-layer stacks of ferromagnets separated by oxide layers[30, 31]

1.3 Motivation for This Work

It is easy to see that magnetic materials and spin-related transport phenomena are the subject of intense study, due to their intrinsic interest and their technological applications[10]. But there are a great many questions remaining regarding the transport of spin in metals, such as the mechanism of spin memory loss and the the spin diffusion length, and spin accumulation at interfaces[32], to name a few. Early work in other spin-dependent transport areas like weak localization theory and universal conductance fluctuations showed values of the spin diffusion length on the order of 1μ m[33]. Is this spin diffusion length the same in

each of these spin dependent phenomena?

In order to make these effects accessible to measurement, it is necessary to design samples whose dimensions match these μ m length scales. It is necessary then to apply the experimental tools of mesoscopic physics to such problems. This work develops a flexible technique for measuring spin related transport phenomena, and presents the successful measurement of a GMR signal in a novel, planar geometry. Moreover, this work explains some of the tools necessary for making such measurements. Experiments such as these require magnetic elements with controllable magnetic properties. For example, elements might be required to have high spin polarization, be single domain with a known axis of magnetization, and have switching fields that can be varied for different structures fabricated in the same process step. These needs dovetail nicely with those of industry[34]. With regard to the recording industry, it is important that the magnetic properties be determined predominantly by the particle shape, thereby reducing particle-to-particle variation due to factors such as grain structure or random magnetocrystalline anisotropy.

In the first part of this work, we outline our approach to producing elements with consistent, controllable magnetic properties. We have chosen an appropriate magnetic material and then introduce a strong shape anisotropy. Co₉₁Fe₉ was chosen due to its desirable thin-film properties: FCC crystal structure[35], low crystalline anisotropy (hence in-plane magnetization), high moment, and moderate coercivity (30 Gauss at 10 K). High-quality films can be produced by dc sputtering, a process which can be made compatible with our e-beam lithographic patterning[36]. Previous studies of other magnetic materials have shown that small, acicular nanostructures with tapered ends are most likely to be single-domain, due to suppression of the flux closure domains present in flat-ended structures[37]. In this work, we employ magnetic force microscopy to determine the domain structure

and switching fields of Co91Fe9 nanoelements of various sizes, and investigate the fabrication steps necessary to produce consistently single-domain elements.

Injection of a spin-polarized current into a nonmagnetic metal and detection of the spin polarization at a distant location dates back to the work of Johnson and Silsbee in 1985. [32] Since that time, attention has shifted to the GMR effect observed in ferromagnetic-nonmagnetic-ferromagnetic (F/N/F) multilayers and spin valve sandwiches.

In the second half of this work we study spin injection and detection in a planar geometry, which allows more flexibility to perform spatially-resolved measurements than is possible in the common sandwich geometries. To do this, we have fabricated F/N/F devices consisting of two single-domain ferromagnetic (F) fingers crossed by a submicron nonmagnetic (N) wire. We report here on the magnetoresistance (MR) of these devices.

This dissertation will be divided into two distinct parts to reflect the two major goals above. Chapters 2,3, and 4 will address the magnetic issues, while Chapters 5,6, and 7 will address the issues of spin-transport. The basis of the analysis in Chapter 2 is the Stoner-Wohlfarth (SW) treatment of single domain particles[38]. Chapter 3 describes the steps taken to fabricate the structures with the desired properties. Chapter 4 contains the experimental results. Chapter 5 will lay out the basics of a spin-dependent transport theory. Chapter 6 will describe the fabrication and measurement of the planar GMR device. Chapter 7 will discuss the results of the transport measurement. Finally, Chapter 8 will include conclusions and discussion of the results, as well as future plans for the experiment.

Chapter 2: Switching in Magnetic

Structures: Background and

Theory

Our primary concerns here are what will determine the domain structure of our magnetic elements, what will determine the direction of magnetization of the elements, and at what field will the direction of magnetization of an element switch. The entire basis for this type of analysis dates back to a seminal paper by Stoner and Wohlfarth [38]. Though this treatment is strictly classical, it holds surprising validity for the behavior of magnetic particles whose dimensions approach the characteristic length scales of spin-related phenomena. The Stoner-Wohlfarth analysis (SW) follows an energy and geometric approach to solve the issues of magnetization direction and switching field. It is this approach that we will follow here.

2.1 Domain Structure

Whether or not a magnetic element is comprised of a single or multiple magnetic domains is determined by the domain wall energy. The domain wall energy is a surface energy associated with the presence of regions separating the individual domains, whose magnetizations are not parallel. The root of this energy is the exchange energy, which is increased as the angle between adjacent magnetic moments is increased. The domain wall energy competes with the energy of the stray fields produced by the magnetic sample. In a single-domain sample, the stray

field energy is quite high, but there is no domain wall energy. In multi-domain samples, there is an increase in domain wall energy along with a corresponding decrease in stray field energy due to the formation of flux closure domain structures within the sample which reduces the stray field. Both of these energies depend on the sample dimensions, with larger samples favoring domain wall formation and smaller samples favoring none. Kittel showed that there is a critical dimension below which the single domain structure will be preffered[39]. Using typical numbers, he shows that for high aspect ratio needles (length:width = 20:1), the critical width was $0.24\mu m$ and the critical length was $4.7\mu m$. Choosing sample dimensions below these values should produce single domain features.

2.2 Magnetization Direction

The remnant state (zero field) magnetization of magnetic particles will be such as to minimize the energy of the system. In this context, we do not need to distinguish between the total energy and the free energy[38]. There are a number of competing energies to be concerned with: magnetocrystalline, strain, and demagnetizing energy. These energies are space dependent, and therefore give rise to anisotropies, or preferred directions of magnetization referred to as easy axes[40]. In the absence of an applied field, the remnant state magnetization will choose between these easy axes. Hysteretic behavior of the resolved magnetization under the application of an external magnetic field will reflect these anisotropies.

2.2.1 Magnetocrystalline Anisotropy

Magnetocrystalline anisotropy is a result of, and contains in it, the symmetry of the magnetic crystal. Or perhaps more correctly, it results from a breaking of spacial symmetry by the presence of the crystal lattice. We have specifically chosen for this experiment to look at ferromagnetic alloys with cubic crystal structures. For cubic crystals the magnetocrystalline energy can be expressed as

$$E_c = K_1(\alpha_1^2 \alpha_2^2 + \alpha_2^2 \alpha_3^2 + \alpha_3^2 \alpha_1^2)[40], \tag{2.1}$$

where α_n is the direction cosine between the magnetization vector and the \hat{x}_n direction unit vector. Typical values for the anisotropy constant K, are shown in Table 2.1. For values of $K_1 > 0$ the energy takes on a minimum at the [100], [010],

Alloy	K ₁ high T	K ₁ low T
$MnFe_2O_4$	-4.0 (290K)	-20 (90K)
$\mathrm{Co_{1.1}Fe_{2.2}O_4}$	380 (300K)	1750 (130K)
CuFe_2O_4	-6 (293K)	-20.6 (77K)
$Zn_{0.30}Fe_{2.70}O_4$	-5.0 (290K)	-21.3(90K)
$\mathrm{Co}_{0.1}\mathrm{Fe}_{0.9}$	34 (300K)	
$\mathrm{Co_{0.4}Fe_{0.6}}$	3 (300K)	
$\mathrm{Co}_{0.5}\mathrm{Fe}_{0.5}$	-11 (300K)	
$\mathrm{Co_{0.7}Fe_{0.3}}$	-42 (300K)	

Table 2.1: List of the magnetocrystalline anisotropy constant for various Fe containing magnetic alloys [40]. K_1 are in units of $10^3 \frac{J}{m^3}$

[001] directions, while for $K_1 < 0$ the energy takes on a minimum at the [111], [111], [111]. These energy minima correspond to the magnetic easy axes.

2.2.2 Strain Anisotropy

Strain anisotropy is the result of magnetostriction, the change of shape of a magnetic specimen during the process of magnetization[40], and is mentioned here only for completeness. Essentially when a sample becomes magnetized, the crystal lattice becomes elongated in the direction of the magnetization. The amount of the deformation, and the increase in strain energy associated with the crystal, will be a function of the orientation of the magnetization relative to the crystal lattice. As such, there will be easy axes associated with the crystal directions which yield

energy minima. In most cases, including this one, the energy scale of the magnetostrictive effect is much smaller than the other energy scales of the problem, and may be neglected.

2.2.3 Shape Anisotropy

Shape anisotropy is determined by the geometry of the magnetic structure. The easy axes are determined by looking at the shape dependent demagnetizing energy. This demagnetizing energy density, E_d , is determined by the scalar product of the magnetization vector, $\vec{M}(\vec{x})$, and the demagnetizing field $\vec{H}_d(\vec{x})$:

$$E_d(\vec{x}) = -\frac{1}{2}\vec{H}_d(\vec{x}) \cdot \vec{M}(\vec{x}). \tag{2.2}$$

Since we are dealing with the case of uniform magnetization, that is, single domain particles, we may write

$$\vec{M}(\vec{x}) = M\hat{m}.\tag{2.3}$$

where M is the magnetization per unit volume and \hat{m} is the unit vector parallel to \vec{M} . The demagnetizing energy, in the absence of free currents, may be calculated using a magnetic scalar potential, $\Phi(\vec{x})$, of the form:

$$\vec{H_d}(\vec{x}) = -\nabla\Phi(\vec{x})[4] \tag{2.4}$$

where

$$\Phi(\vec{x}) = \oint \frac{\vec{M}(\vec{x}') \cdot \hat{n}'}{|\vec{x} - \vec{x}'|} da' - \int \frac{\nabla' \cdot \vec{M}(\vec{x}')}{|\vec{x} - \vec{x}'|} d^3x'$$
 (2.5)

Since \vec{M} is constant inside the region of integration, the volume integral drops out, and only the surface integral survives, and Equation 2.5 reduces to

$$\Phi(\vec{x}) = \oint \frac{\vec{M} \cdot \hat{n}'}{|\vec{x} - \vec{x}'|} da'. \tag{2.6}$$

substituting Equations 2.6, 2.3, and 2.4 into Equation 2.2 gives

$$E_d(\vec{x}) = \frac{1}{2} M^2 \hat{m} \cdot \nabla \oint \frac{\hat{m} \cdot \hat{n}'}{|\vec{x} - \vec{x}'|} da'. \tag{2.7}$$

We now have a form for the energy density as a function of position everywhere inside an arbitrary shape for a uniform magnetization. It is proportional to the square of the magnitude of the magnetization. Additionally there is a factor that is completely geometric in nature. To continue, it is necessary to commit to a specific geometry. However, general solutions to Equation 2.7 are not possible for all shapes. In fact, only closed surfaces of the second kind (in particular, ellipsoids) are possible. It turns out, however, that a great many shapes may be approximated with good accuracy by these solutions. The mathematics of such a solution are nonetheless complex, but are well known[41][42]. With these solutions we may write the demagnetizing energy per unit volume as

$$E_d = \frac{1}{2}M^2(N_a\alpha_a^2 + N_b\alpha_b^2 + N_c\alpha_c^2),$$
 (2.8)

where a, b, and c are the lengths of the semi-major axes of a general ellipsoid, α_n are the direction cosines between the direction of magnetization and the principal axes of the ellipsoid, and N_n are called the demagnetizing factors along these axes[38]. These demagnetizing factors obey the rule

$$N_1 + N_2 + N_3 = 4\pi. (2.9)$$

The forms for N may be given as the following [42], using the reduced variables $\beta = \frac{b}{a}$ and $\gamma = \frac{c}{a}$:

$$\frac{N_a}{4\pi} = \frac{\beta\gamma}{(1-\gamma^2)^{\frac{1}{2}}(1-\beta^2)} [F(k,\theta) - E(k,\theta)]$$
 (2.10)

$$\frac{N_b}{4\pi} = \frac{\beta\gamma}{(1-\gamma^2)^{\frac{1}{2}}(1-\beta^2)} \left[-F(k,\theta) + \frac{1-\gamma^2}{\beta^2-\gamma^2} E(k,\theta) + \frac{\gamma(1-\beta^2)(1-\gamma^2)^{\frac{1}{2}}}{\beta(\beta^2-\gamma^2)} \right]$$
(2.11)

$$\frac{N_c}{4\pi} = \frac{\beta\gamma}{(1-\gamma^2)^{\frac{1}{2}}(\beta^2-\gamma^2)} \left[\frac{(1-\gamma^2)^{\frac{1}{2}}\beta}{\gamma} - E(k,\theta) \right]$$
 (2.12)

where $E(k,\theta)$ and $F(k,\theta)$ are elliptic integrals of the first and second kind, where

$$k^2 = \frac{1 - \beta^2}{1 - \gamma^2} \tag{2.13}$$

and

$$\sin^2 \theta = 1 - \gamma^2. \tag{2.14}$$

2.2.4 Comparison of Anisotropy Energies

The energy scale of the magnetocrystalline anisotropy was set by the constant K_1 given in Table 2.1. The energy scale for the shape anisotropy is set by the value of M in Equation 2.8, which are given in Table 2.2. If we compare the values in the

Alloy or Metal	M^2
Fe	23.2
78 Permalloy	5.88
Supermalloy	3.14
$\mathrm{Co_{50}Fe_{50}}$	30.2

Table 2.2: List of the magnetization energy densities, $M^2[43]$. Numbers are in units of $10^3 \frac{J}{m^3}$

two tables, we see that the energy scales set by the two anisotropies are similar, with the exception of the cobalt-iron oxide listed in Table 2.1, which possesses unusually strong crystalline anisotropy. The suggestion here is, however, that careful choice of material (low crystalline anisotropy, high saturation magnetization) and shape could be used to fix the direction of magnetization in small magnetic structures.

2.2.5 Acicular Nanoelements

For structures in this work, we may use the forms for N in Equations 2.10,2.11, and 2.12, and set $a > b \gg c$, or $\beta \gg \gamma, 1 \gg \gamma$. In this case we may reduce the arguments of the elliptic integrals to

$$k \longrightarrow m = 1 - \beta^2 \tag{2.15}$$

and

$$\theta \longrightarrow \frac{\pi}{2}.$$
 (2.16)

In this case $F(k,\theta)$ and $E(k,\theta)$ become K(m) and E(m), the complete elliptic integrals of the first and second kind. Substituting them into the appropriate equations along with the appropriate approximations, the demagnetizing factors reduce to

$$\frac{N_a}{4\pi} = \frac{\beta\gamma}{1-\beta^2} [K(m) - E(m)] \tag{2.17}$$

$$\frac{N_b}{4\pi} = \frac{\beta \gamma}{1 - \beta^2} \left[\frac{1}{\beta^2} E(m) - K(m) \right]$$
 (2.18)

$$\frac{N_c}{4\pi} = 1 - \frac{\gamma}{\beta} E(m). \tag{2.19}$$

Where the argument $m=1-\beta^2$.

2.2.6 Meaning of Demagnetizing Factors

The physical origin of the demagnetizing factors comes from looking at the demagnetizing field generated inside bodies with uniform magnetization. When a body is uniformly magnetized, there will be on the outer surface free poles, whose density is given by the numerator in Equation 2.6. Those poles are analogous to the charges on a capacitor, and generate a magnetic field inside the sample. For instance, in the case of a flat sheet whose thickness is much less than the lateral

dimensions, we might see something like Figure 2.1. The magnitude of the demagnetizing field is given as

$$H_D = -\sum D_i M_i \tag{2.20}$$

where D_i are the demagnetizing factors, and are related to the N_i by

$$D_i = \frac{N_i}{4\pi}. (2.21)$$

We've already worked out the demagnetizing factors for the general ellipsoid, which provides an excellent general form which provides a good approximation to many shapes. It is instructive, however, to look at some limiting cases of the ellipsoid. In fact, using the normalization of the demagnetizing factors given by Equation 2.9 we may infer the values of D for some useful geometries.

Start with the case of a long, narrow cylinder. If we let the magnetization lie parallel to the long axis, the poles are formed on the circular ends, but not on the sides. Using the analogy of the charged capacitor plates we know that the field will go as the inverse of the distance between the plates. So, if the length of the cylinder goes to infinity, the field induced by the poles will go to zero, which implies that the demagnetizing factor (H=DM) must go to zero. The remaining two factors lie in the plane of the circular cross-section of the cylinder. The two factors must therefore be equal, and therefore due to the sum rule each equal to $\frac{1}{2}$.

In the case of the infinite sheet shown in Figure 2.1, the directions in the plane see poles way out at infinity, and therefore the demagnetizing factors must be equal, and equal to zero. In the direction perpendicular to the plane, the sum rule dictates that the remaining factor is equal to 1.

Finally, in the case of the the sphere, each of the factors must be equal, and the sum rule dictates that they be equal to $\frac{1}{3}$. The demagnetizing factors for each of the

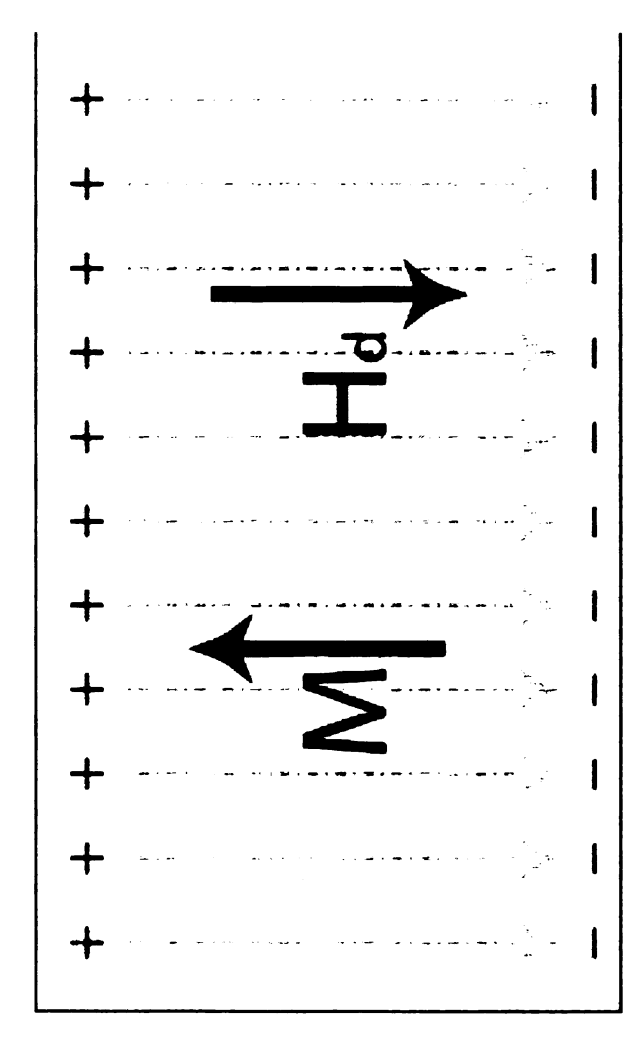


Figure 2.1: Schematic representation of the origin of the demagnetizing field in the case of the infinite sheet. The poles on either surface produce a magnetic field in manner analogous to the electric field do to charges on the plates of a capacitor.

preceding limiting cases are listed in Table 2.3.

	D_a	D_b	D_c
Long Cylinder	0	$\frac{1}{2}$	$\frac{1}{2}$
Flat Sheet	1	0	0
Sphere	$\frac{1}{3}$	$\frac{1}{3}$	$\frac{1}{3}$

Table 2.3: The demagnetizing factors for the limiting cases of the long cylinder, the flat sheet, and the sphere.

So, apparently in the case of a magnetic sample, in directions where the sample dimension is small, the demagnetizing factor is large, and from equation Equation 2.8 so to will be the demagnetizing energy. In a similar manner, where the dimension is large, the demagnetizing factor is small, and so to will be the demagnetizing energy. As an example, if one desired to control the magnetization direction of the small sample, by choosing a metal with low crystalline anisotropy and making the sample shape long and slender, it should be possible to force the magnetization to lie parallel to the long axis.

2.3 The Switching Field

To calculate a form for the switching field we must look to the Stoner-Wohlfarth method. We begin by looking at the total energy of a uniformly magnetized ellipsoid in an external field. The total energy will have a term that corresponds to the demagnetizing energy and a term that corresponds to the external field and the magnetization:

$$E_{total} = E_{external} + E_D. (2.22)$$

Substituting Equation 2.8 into Equation 2.22 gives

$$E_{total} = -\vec{M} \cdot \vec{H} + \frac{1}{2}M^2(N_a\alpha_a^2 + N_b\alpha_b^2 + N_c\alpha_c^2).$$
 (2.23)

If $c \ll a, b$ then the magnetization will rotate in the plane of the sample, and we may take $\alpha_c = 0$, $\alpha_a = \cos \theta$, $\alpha_b = \sin \theta$, and

$$E_{total}(\theta, H) = HM \cos \theta + \frac{1}{2} M^2 \{ N_a \cos^2 \theta + N_b (1 - \cos^2 \theta) \}.$$
 (2.24)

The first term on the right hand side represents the field energy, where the field has been applied parallel to the a-axis, but in the negative direction. The angle θ is the angle between the magnetization, \vec{M} , and the positive a-axis. The two terms in the energy compete, with the field energy wishing to flip the magnetization to the negative direction, while the second term presents an energy barrier to such a rotation.

Looking at the form of Equation 2.24, we know that when H is zero, the slope of the function $E(\theta, H)$ for small positive θ will be positive (the magnetization sees a hill to climb). As H is increased from zero, the hill is lowered, and the slope at $\theta = 0$ is reduced. At the critical field, the slope of $E(\theta, H = H_c)$ will equal zero. Moreover, the second derivative of $E(\theta, H = H_c)$ is negative, meaning that that the magnetization is in an unstable equilibrium. At this point the magnetization may spontaneously switch. Plots of Equation 2.24 in units of E/M^2 for several values of H are shown in Figure 2.2.

To calculate the value of H_c it is only necessary to take the derivative of Equation 2.24 with respect to θ and set it equal to zero:

$$\frac{\partial E_{total}}{\partial \theta} = 0. {(2.25)}$$

Solving Equation 2.25 for H and setting $\theta = 0$ gives

$$H_c = M(N_b - N_a). (2.26)$$

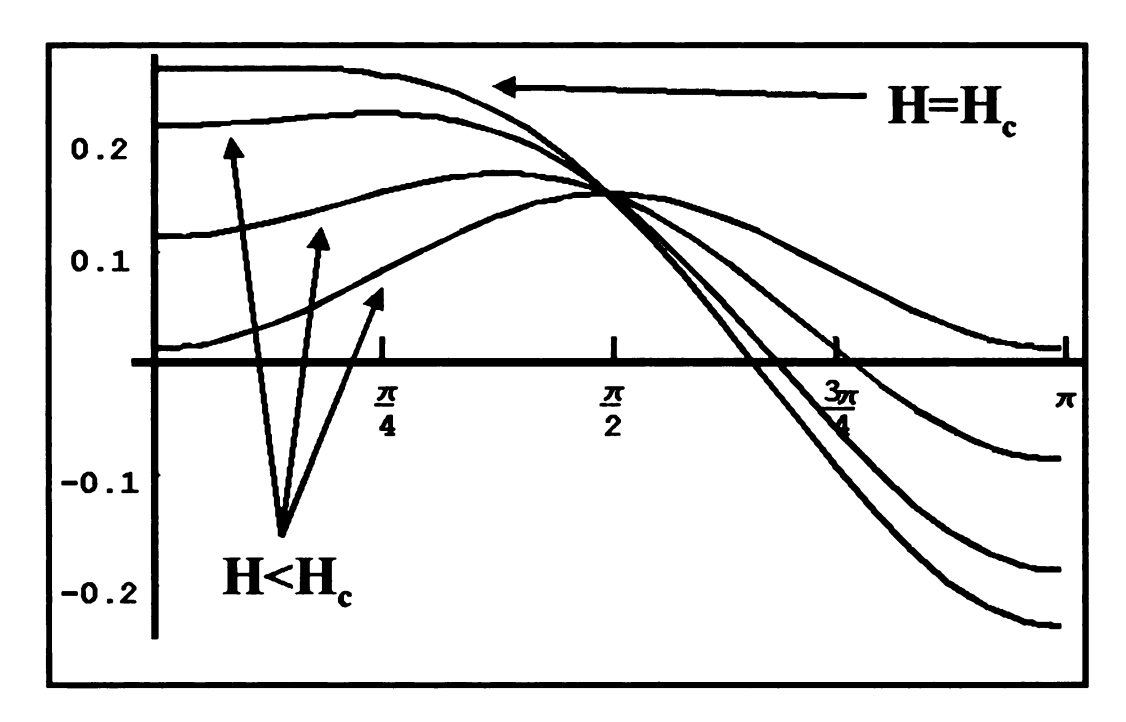


Figure 2.2: Plots of the total energy as a function of θ of a magnetized ellipsoid for several values of the applied external magnetic field. The vertical axis is in units of E/M^2

Substituting in the forms of N from Equation 2.17 and Equation 2.18, gives

$$H_c = 4\pi M \left(\frac{\beta \gamma}{1 - \beta^2} \left[\frac{1}{\beta^2} E(m) - K(m) \right] - \frac{\beta \gamma}{1 - \beta^2} \left[K(m) - E(m) \right] \right). \tag{2.27}$$

This reduces to

$$H_c = 4\pi M \frac{c}{b} \left[\frac{(1+\beta^2)E(m) - 2\beta^2 K(m)}{1-\beta^2} \right]. \tag{2.28}$$

Rewriting Equation 2.28 in terms of m,

$$H_c = 4\pi M \frac{c}{b} \left[\frac{(2-m)E(m) - 2(1-m)K(m)}{m} \right]. \tag{2.29}$$

The quantity $\frac{(2-m)E(m)-2(1-m)K(m)}{m}$ from Equation 2.28 is plotted in Figure 2.3. In most samples considered in this work, $a \approx 10b$. This gives m=.99, for which the quantity plotted in Figure 2.3 is essentially 1.

Thus the functional form for the ellipsoid of revolution with $a > b \gg c$ reduces

for our samples to the simple form:

$$H_c = 4\pi M \frac{c}{b}. (2.30)$$

It is not entirely unexpected that the energy barrier to switching would go as the inverse of the width. This is because as the element becomes narrower, the demagnetizing energy associated with the magnetization parallel to the b-axis grows larger. What is surprising, perhaps, is the lack of dependence on a. In fact, it would seem logical that the final result would have contained the quantity $\frac{b}{a}$, which is the aspect ratio of ellipsoid. However, we have essentially eliminated the a dependence in our sample by letting the aspect ratio grow very large. Finally, there is the surprising existence of c in the final form. The value of c is the thickness of the flat ellipsoid. On first inspection it would have seemed that our requirement of rotation in the plane would have eliminated any c dependence. This, however, is also a natural consequence of the demagnetizing factors. Recall that the demagnetizing factors must add to a constant value, and that the demagnetizing factor in a given direction decreases as that corresponding length increases. So as the thickness of the sample increases, its associated demagnetizing factor decreases, and returns some of that to the total. Since the width is quite a bit less than the length, it evidently absorbs the majority of that which has been returned, thereby increasing the effective energy barrier to rotation.

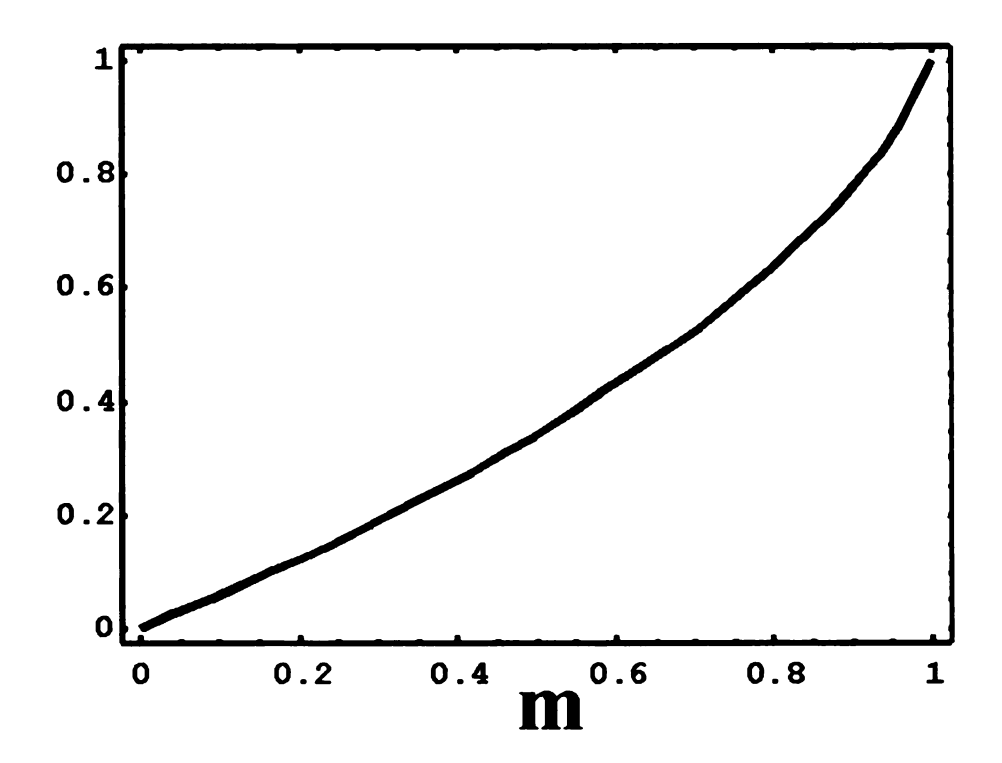


Figure 2.3: Plot of the quantity $\frac{(2-m)E(m)-2(1-m)K(m)}{m}$ as a function of m.

Chapter 3: Switching in Magnetic

Structures: Experimental

Procedure

3.1 Electron Beam Lithography

In order to pattern elements of the required size (on the order of 100nm), we required the use of electron-beam lithography (EBL)[44]. EBL is a form of lithography whereby a thin polymer layer is exposed to an electron beam inside of a scanning electron microscope. That resist layer is thereby made soluble to a developer. The development process preferentially removes the exposed resist, leaving a polymer layer that covers the surface of the substrate, with the substrate uncovered in only the desired pattern. Figure 3.1 shows the process in a highly generalized form. In principle, any new experiment will require some revision of the general EBL procedure. Our specific procedure is indicated in Table 3.1.

Spin	9% P{MMA/MAA}	4000 rpm	40s
Bake		150°C	60min
Cool			
Spin	2% 450K PMMA	4000 rpm	40s
Bake		150°C	60min
Cool			
Expose			
Develop	MIBK:IPA 1:3	23°C	60S
Rinse	IPA		20S
Rinse	DI		20S
Metalize			
Liftoff	Acetone	60°C	1 hour

Table 3.1: Recipe used to produce the EBL features.

Analysis of Table 3.1 indicates that two layers of resist are spun onto the substrate. The first layer, a co-polymer of polymethylmethacrylate and methylacrylic acid (P{MMA/MAA}), is more sensitive to the electron beam than is the upper polymer layer of Polymethylmethacrylate (PMMA). The purpose of this is to generate an undercut in the resist profile. After exposure, as development commences, the developer begins to erode the pattern over which the beam has been written. As the top layer clears, the developer begins to aggressively attack the second layer at a rate much greater than that of the top. This leads to the desired undercut. Figure 3.2 shows the result of the undercut produced by such a bilayer. The purpose of the undercut is to ensure clean lift-off. Lift-off commenses after the desired post-development processes. These are most generally metalization. Were we not to use an undercut resist profile, the deposited metal would climb the walls of the developed portion of the resist, resulting in a number of undesired effects. These might include incomplete lift-off of the resist or sharp vertical peaks along the edges of the resulting metal features.

3.1.1 Specific Notes Regarding Electron Beam Lithography

The EBL for this experiment was done using a JOEL JSM 840 equiped with a tungsten hairpin filament. Typical operating parameters for the microscope are listed in Table 3.2. In general, each batch of samples prepared will require a test

Accelerating Voltage	35keV
Course Beam Current	10pA
Measured Beam Current	5pA to 6pA
Line Dose	$0.9 - 1.1 \frac{nC}{cm}$
Area Dose	$150 \frac{\mu C}{cm^2}$

Table 3.2: These are the operating parameters used in the JOEL JSM 840 scanning electron microscope for a typical writing.

sample, where a variety of line and area doses are written, the sample developed and

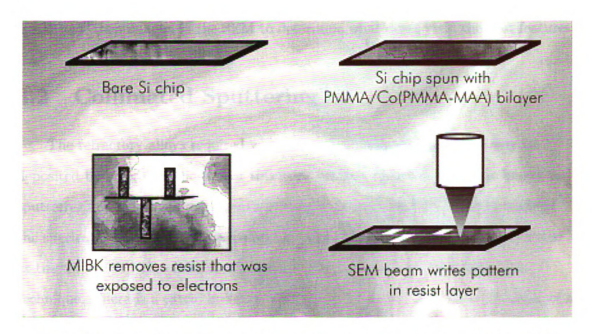


Figure 3.1: Generalized representation of the processing steps involved in EBL.

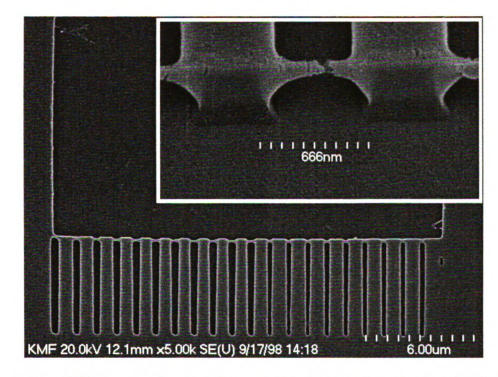


Figure 3.2: SEM image showing the resist undercut of a developed bilayer of P{MMA/MAA} and PMMA. The main image is the top view of a large box, below which a series of lines have been written. The lines are left short of the box to minimize widening of the undercut from proximity effect exposure due to the box itself. The inset in the upper right corner is looking at the edge between the box and the lines with the substrate tilted.

metallized, then imaged in the SEM to determine what doses yield the best features.

3.2 Collimated Sputtering

The refractory alloys required when using ferromagnetic materials may be deposited by several methods. For this work we have chosen a technique known as sputtering. Sputtering is a momentum-transfer process whereby a target made of the species to be deposited is assaulted by argon ions which have been accelerated at the target [45]. Excellent stoichiometric alloys can be produced using this technique. There is a catch, however. Due to the relatively high pressure inside of a sputtering chamber the sputtered species has a very short mean free path. As a result, the substrate onto which we are sputtering sees an isotropic distribution of incident momenta. If sputtering were performed in this manner the undercut provided by the bilayer process would be insufficient to prevent coating of the side walls. Therefore, a collimating body, pictured in Figure 3.3 is used. The collimator is fabricated from stainless steel and is built to be compatible with the sputtering chamber to be used. The critical dimensions of the collimator are the length of the collimator, and the bore diameter of the long tube through which the sputtered atoms will travel. For this particular collimator the inner bore is 0.08in and the length is 0.40in. This body limits the momenta of incident momenta to those which fall within some small range around the substrate normal. By doing so, the resist undercut may adequately prevent deposited metal from coating the resist sidewalls. It must be noted that the reduction in incident particles is accompanied by a reduction in deposition rate at the sample. Longer sputtering times are therefore necessary to produce desired thicknesses. Actual deposition rate is measured by AFM topographic analysis (see Section 3.3).

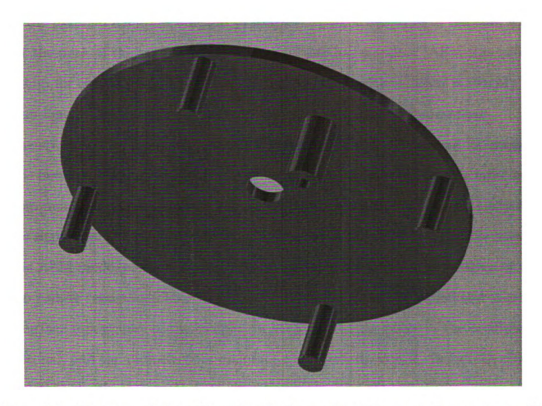


Figure 3.3: Diagram of the collimating body used in the sputtering process. The four smaller posts are for mechanical manipulation of the body inside the sputtering chamber. The larger, single post has a hole bored parallel to the long axis which limits the range of momenta of incident atoms that reach the substrate to a small number around perpendicular.

3.3 Magnetic Force Microscopy

Magnetic force microscopy (MFM) is a modified form of atomic force microscopy (AFM) where the tip has been coated with a magnetic alloy, and operates in a similar manner. In AFM, the microscope consists of a micromachined silicon pyramid placed on the end of a cantilever. From Figure 3.6, one can deduce that the pyramid itself has a height of roughly $10\mu m$. The radius of the tips, which lie at the peak of the pyramid, is roughly 0.020 µm for 'standard' AFM tips and $0.050\mu m$ for coated MFM tips. From Figure 3.5, the cantilever itself is roughly $125\mu m$ long. During normal operation the tip is oscillated at its resonant frequency, which for standard tips is between 100kHz and 300khz, and for magnetic tips is between 50kHz and 100kHz. As the tip scans the surface, a laser reflected off the tip monitors its oscillation. Interactions between the tip and sample surface cause slight changes in the oscillation. In the case of standard topographic scanning in the AFM mode, piezoelectrics in the tip holder alter the vertical position of the tip to restore resonance. These changes in the tip height are recorded and mirror the surface topography of the sample. In MFM mode, the phase of the oscillation is monitored, and the piezoelectrics maintain a constant tip height. In fact, in order to insure that the tip to sample distance remains constant throughout the scan, each scan line is first made in topographic mode, then followed immediately by a phase scan with the tip lifted to a height determined by the user. In this way, when the phase of the oscillations shifts, it can be attributed solely to the magnetic interaction between the tip and sample. This phase shift corresponds to changes in the derivative of the perpendicular component of the magnetic field.

$$\Delta\phi \propto \frac{\delta H_z}{\delta z} \tag{3.1}$$



Figure 3.4: An SEM image of an AFM tip.



Figure 3.5: An SEM image of an AFM tip, this time closer up.

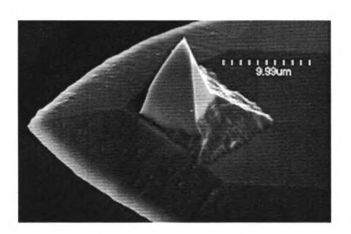


Figure 3.6: An SEM image of an AFM tip, really up close.

From Equation 3.1 we can deduce that in regions where the field points up, the phase shift will be of opposite sign to those areas where the field points down.

Figure 3.7 shows a cartoon representation of the stray field from a magnetic sample and the MFM tip.

A sample MFM image is shown in Figure 3.8. The left hand box shows a topographic scan of a square 1μ m on a side. The center box shows the phase channel image acquired at a lift height of 50nm. The right hand side shows a schematic view of the direction of magnetization. This square is single-domain. Note in the center box that areas of light contrast correspond to uncompensated north poles, while darker areas correspond to uncompensated south poles.

Figure 3.9 shows another square, this one $12\mu m$ on a side. Here there is contrast all through the bulk of the square, indicating the presence of domain structure throughout.

3.3.1 Limitations of Magnetic Force Microscopy

In principle, a phase channel map is not unique. Indeed there are an infinite number of magnetic configurations that will yield any given magnetic scan. However, in cases where symmetry dictate that only certain solutions are appropriate, a unique solution can often be inferred. Also, the tip, also being magnetized, exerts an equal force onto the sample. In cases of soft magnetic materials, it is possible that the imaged phase map is not the actual remnant state domain structure. Instead, as the tip scans the surface the local domain structure is altered in the region of the tip, generally resulting in a net attraction between the tip and sample.

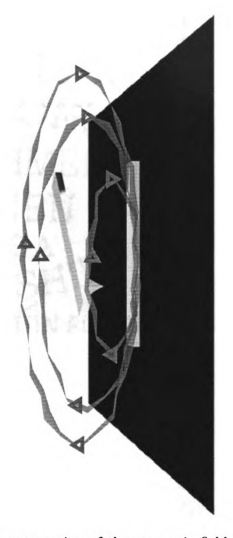


Figure 3.7: A cartoon representation of the magnetic field from the sample and the MFM tip.

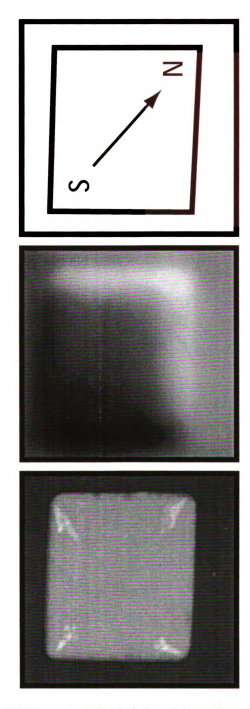


Figure 3.8: A sample MFM image. The left hand box shows a topographic scan of a square $1\mu m$ on a side. The center box shows the phase channel image acquired at a lift height of 50mm. The right hand side shows a schematic view of the direction of magnetization. This square is single-domain. Note in the center box that areas of light contrast correspond to uncompensated north poles, while darker areas correspond to uncompensated south poles.

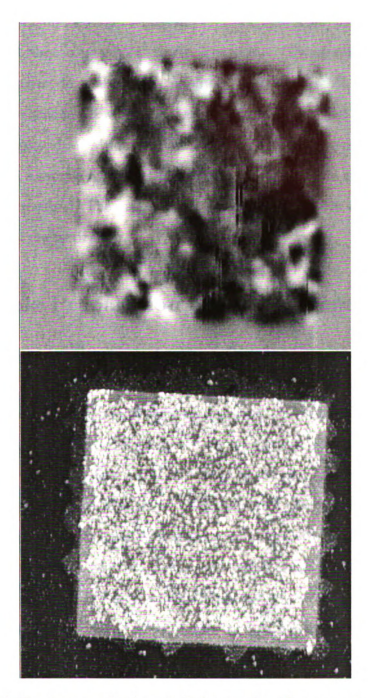


Figure 3.9: This is a topographic/magnetic image of a $12\mu m$ square. The left hand image is the topographic, the right hand image is the magnetic. Here you clearly see areas of contrast in the bulk of the square, indicating a multi-domain sample.

3.3.2 Specific Notes Regarding Magnetic Force Microscopy

The MFM measurements presented in this work were made using a Digital Instruments 3100 Nanoscope with Extender Electronics. Topographic scans were done using tapping mode, with an rms amplitude of 2.00 volts, 5% offset. It is also important to note that in MFM all scans are made at zero applied field. In this work we have employed MFM for magnetometry experiments in which an external field is applied to a sample outside of the microscope, the sample is remounted and the MFM image acquired. The magnetization images produced in this way are of the remnant state magnetization.

3.4 Sample Preparation and Measurement

To fabricate the samples, we start with 3in $\langle 110 \rangle$ Si wafers, which are diced into chips $\frac{1}{2}$ in square. These chips are prepared for EBL using the recipe in Table 3.1. In the SEM we write various arrays of elements, varying the length and width. After development, $Co_{91}Fe_9$ is sputtered using the collimator in Figure 3.3. Lifting off reveals arrays of $Co_{91}Fe_9$ fingers which are ready for characterization.

To measure the samples, a series of MFM images is acquired. Each image shows the remnant state (zero field) magnetization of the arrays, after a field has been applied using a small solenoid magnet, pictured in Figure 3.10. The solenoid is made from light gauge copper wire, with as many turns as would be accommodated by the teflon spindle. The inner bore of the spindle is slightly larger than the 0.5in square Si substrates used in the experiment. The solenoid was calibrated using a flux gate magnetometer and was found to have a coil constant of $220\frac{Oersted}{Ampere}$ The field is applied parallel to the long axes of the fingers, and the magnitude is incremented and decremented to various values. Continuing in this way we may count the fraction of the fingers for each given size that have flipped as a function of

the field applied.



Figure 3.10: Representation of the homemade solenoid magnet used in the switching field characterization experiments. The inner bore of the magnet is 0.5in, and the overall length is 3.0in.

Chapter 4: Switching in Magnetic Structures: Experimental Results

4.1 Fabrication of Single Domain Elements

4.1.1 $Co_{91}Fe_9$ Thin Films

In order to achieve the desired magnetic properties, we must choose an appropriate magnetic material. We seek a material that will provide us with a good spin polarization, but whose crystallographic properties won't interfere with our efforts to control the magnetization of the samples using shape anisotropy. Thin films studies on films produced here at MSU suggested that Co₉₁Fe₉ would be a good candidate. Co₉₁Fe₉ is a cubic crystal with low crystalline anisotropy. Contrast this with, say, pure Co, which tends to grow as a hexagonal close-pack (hcp) crystal, and possesses a strong magnetocrystalline anisotropy which encourages the magnetization to point out of the plane of the film.

 $Co_{91}Fe_{9}$ thin films also show high saturation magnetization and large coercive fields. Figure 4.1 shows a SQUID magnetometer measurement of a 30nm thick $Co_{91}Fe_{9}$ thin film.

A concern when using refractory metals is the effect of oxygen exposure. Many magnetic alloys form oxides that can have perverse effects on the magnetization. Often the oxide layer is anti-ferromagnetic, and causes anomalous hysteresis effects. One way to combat this is to cap the ferromagnetic metal with a protective layer of inert metal, such as Au, or a metal such as Al that forms a very thin native oxide which protects itself from further oxidation. Figure 4.2 shows a series of Co₉₁Fe₉ films with various thickness of Al capping layers. Those films with adequate

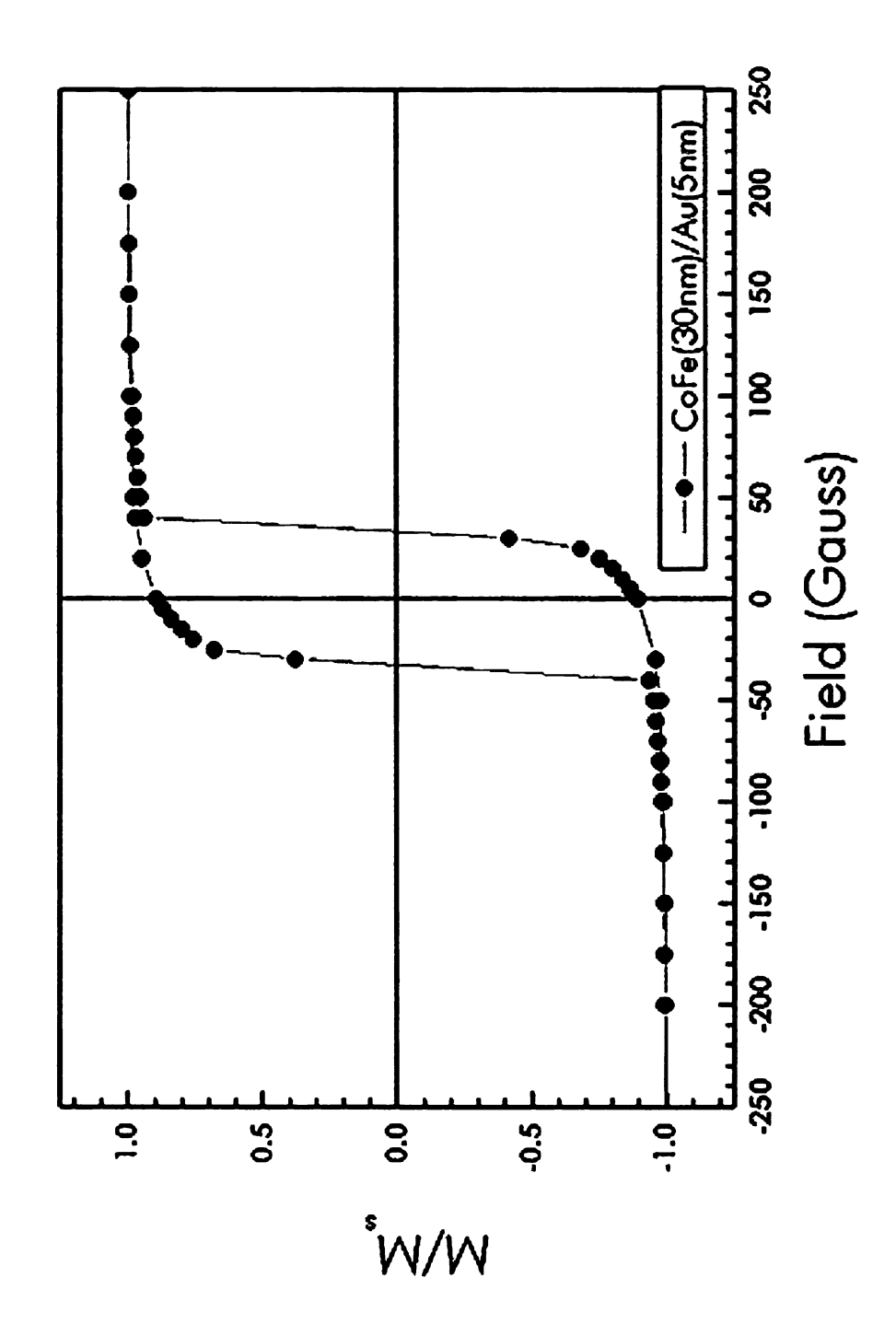


Figure 4.1: A SQUID measurement of a 30nm Co₉₁Fe₉ thin film.

protection, such as that with the 2.5nm thick Al layer, exhibit normal hysteresis, with sharp transitions at the coercive fields. As the Aluminum becomes thinner, the hysteresis curve becomes flatter, until the case where there is no Al at all, and the unprotected film exhibits strong flattening.

One final concern is how will the thin film properties of Co₉₁Fe₉ hold up under collimation. This might not seem like a concern initially, however in all physical vapor deposition processes, the exact conditions of the deposition play directly into the quality and properties of the deposited film. The collimator itself not only changes the distribution of incident momenta (see Section 3.2) but it will greatly lower the sputtering rate as well. In order to verify the thin film properties, several collimated films received SQUID analysis. Figure 4.3 shows two hysteresis curves for collimated thin films. They show good hysteresis.

4.1.2 Co₉₁Fe₉ Nanostructures

Now that we have a suitable thin film candidate, it is necessary to check that the resulting nanostructures fabricated from $Co_{91}Fe_9$ can indeed be made single domain, and have a controllable direction of magnetization. Using the arrays discussed in Section 3.4, we can image the virgin state magnetization in the MFM. Figure 4.4 and Figure 4.5 show the Topographic and MFM images of protected and unprotected $Co_{91}Fe_9$ arrays, respectively. The fingers in both figures are 15nm thick. The three distinct groupings represent different width fingers. The top group are fingers with a width of 0.25μ m. The middle group has fingers of 0.17μ m, while the last group has widths of 0.10μ m. Within each grouping are fingers of lengths 0.5, 1.0, 2.0, and 4.0μ m, except for the thinnest grouping, where the 4.0μ m length has been omitted. Notice that Figures 4.4 and 4.5 are consistent with our thin film data from Figure 4.2. Like the protected thin films, the nanostructures which have been coated with gold are indeed single domain, while those left unprotected have

43

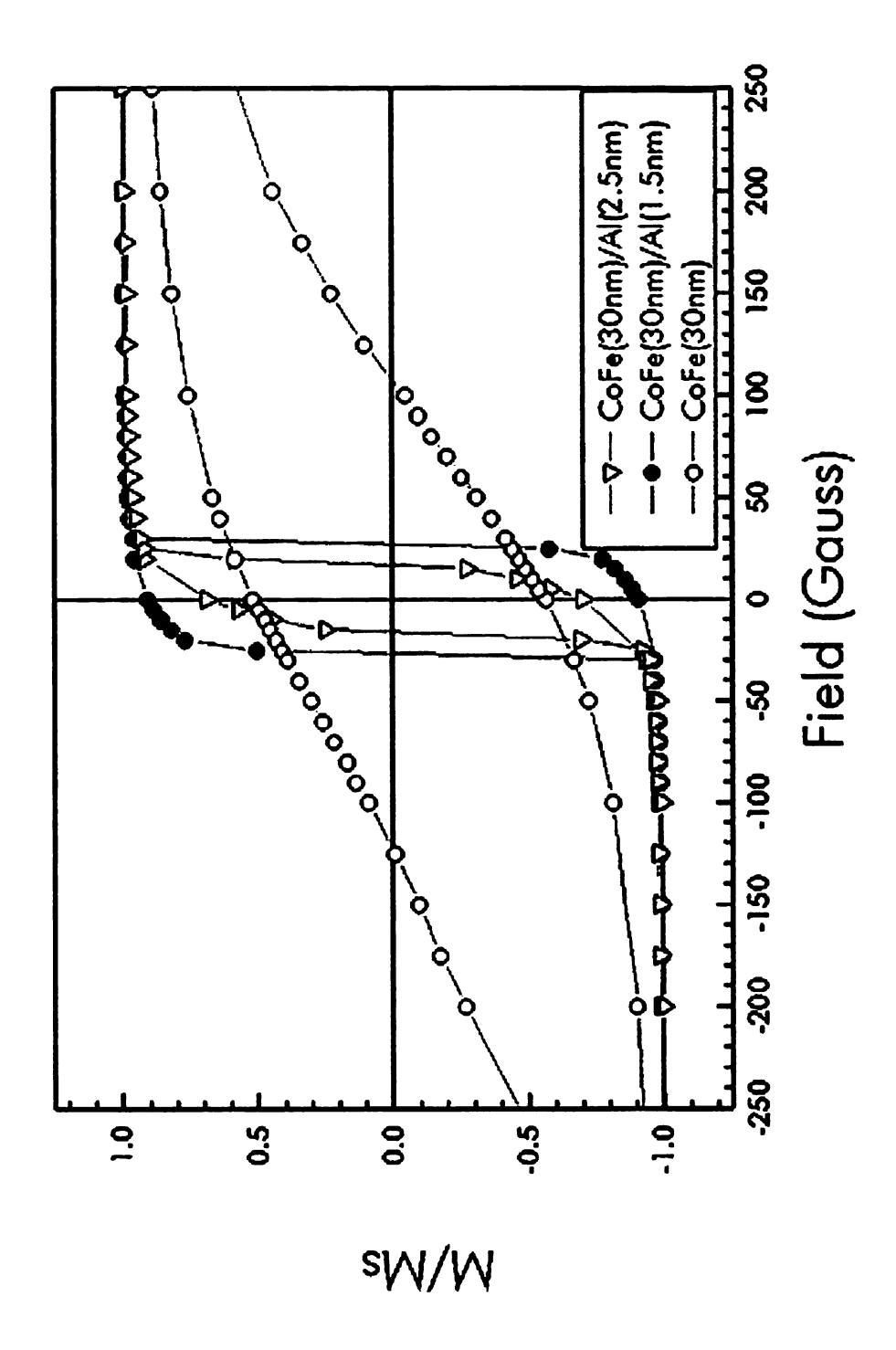


Figure 4.2: SQUID measurements of various thin films. Those films whose Al capping layer were inadequate suffered from environmental oxidation. This results in a flattening out of the hysteresis curve.

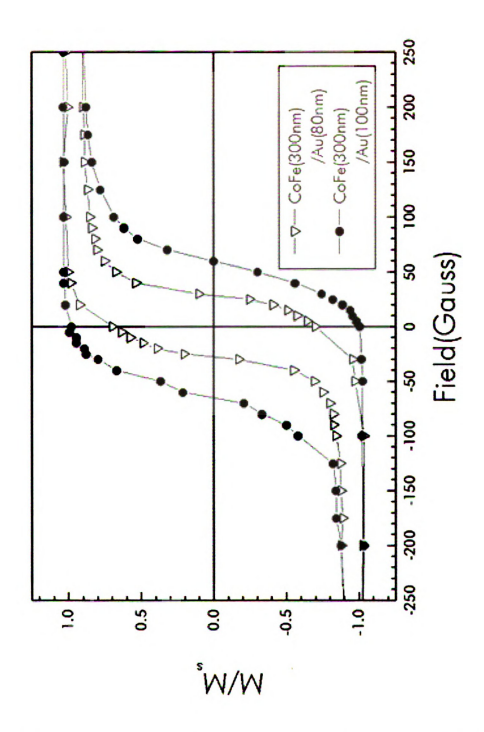


Figure 4.3: SQUID measurements of collimated $Co_{91}Fe_{9}$ thin films. The films are thinner than the amount in the legend by about a factor of 20, due to the collimator. Actual thickness was determined via AFM topographic scan. The shape of the hysteresis curves is good.

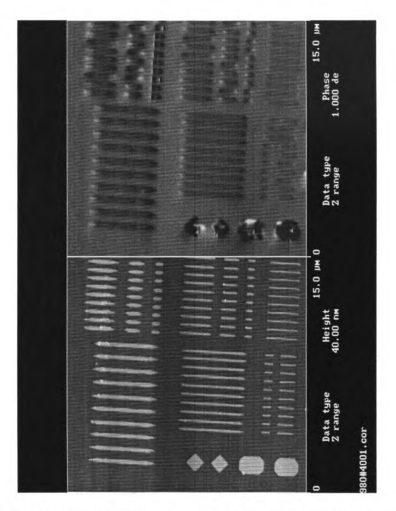


Figure 4.4: Topographic and MFM scans of 20nm thick Co₉₁Fe₉ fingers of various lengths and widths. These fingers have been protected with a thin layer of Au, and are therefore protected from environmental oxidation. As such they are single domain, with their magnetization parallel to their long axis, which is indicated by the light and dark contrast on the ends, with no contrast interior to the fingers.

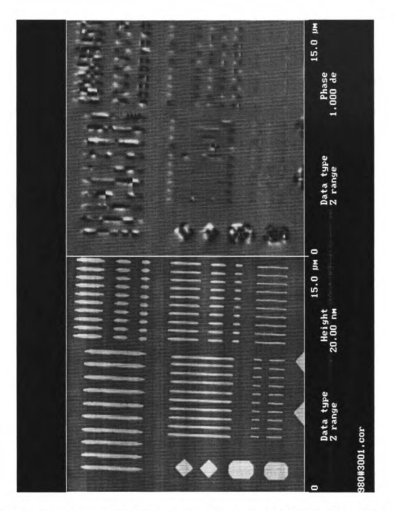


Figure 4.5: Topographic and MFM scans of 20nm thick Co₉₁Fe₉ fingers of various lengths and widths. These fingers have been left unprotected, and therefore exhibit the effects of environmental oxidation, which results in the domain structure interior to the fingers.

formed domain structure interior to the fingers themselves. We interpret this as due to the existence of a native oxide layer that forms in the unprotected case.

Figure 4.4 also confirms our expectation that the fingers that remain single-domain indeed have their magnetization pointed parallel to their long axis.

One point of interest is that in the case of the unprotected fingers of Figure 4.5, some of the fingers have remained single-domain in spite of the oxidation. Notice too, that the effect of shape-anisotropy is actually dependent upon the aspect ratio of the finger. However, the tendency to remain single domain actually correlates with the width of the finger. Those in the bottom group, which are thinnest, are almost all single-domain. Those in the progressively wider groups exhibit a progressively greater tendency to break into domains.

4.2 Controlling the Switching Field

Through our judicious choice of material and geometry, we have shown that we can indeed produce magnetic features which are single-domain with a known direction of magnetization. Now the question is, what about when we apply an external magnetic field? When will a finger decide to switch its direction of magnetization? Can the shape of the fingers be made so that there are fingers with different switching fields? Proceeding in the manner described in Section 3.4, we can apply a series of external fields of different values to an array of such single-domain fingers. The field is applied parallel to the long axis, and after each application, the remnant state magnetization is imaged in the MFM. First, in Figure 4.6 the top most image in each column is a topographic scan of two different width fingers. The second row shows the corresponding MFM image of the virgin state magnetization. The third row shows MFM images of the same fingers after application of an 800Gauss field parallel to the long axis of the fingers, and directed upward on the

page. In the virgin state images, the fingers have randomly oriented magnetizations. After application of the field, all the fingers, in both widths, have aligned themselves with the field (light contrast represents the north poles).

After application of the large field in the upward direction, we may now continue and apply successively larger fields in the opposite direction. In Figure 4.7, the top most image in each column shows MFM images of the same fingers from Figure 4.6 after application of an 800 Gauss field parallel to the long axis of the fingers, and directed upward on the page. The second row of pictures shows the same fingers after application of an external magnetic field of 440 Gauss directed downward on the page. The third row shows the same fingers after the field has been increased to 570 Gauss. Notice that after application of the 440 Gauss field, all of the wider fingers have reversed their magnetization, while only 1 of the narrower fingers has. Furthermore, after the field is increased to 570 Gauss, several additional narrow fingers have switched. Continuing in this way with more field values and more widths and lengths, we may plot the average number of fingers of a given length and width that have switched as a function of the applied field. The results are shown in Figure 4.8. Here you see that the different widths separate themselves into two distinct groups with different switching fields. This is consistent with previous results[46, 47, 48, 49].

It is also of interest to compare the switching fields thus measured to the theoretical prediction of Equation 2.30. The results are summarized in Table 4.1. The table was constructed using a sample thickness of 15nm and a saturation magnetization (M) of 1500 Gauss. Notice that the calculated numbers are larger than the measured by about a factor of 3, but the ratio of measured switching field between the wide and narrow samples agrees with the calculated ratio. That our measured values deviate from those calculated from the mathematically perfect ellipsoid is not discouraging. Our elements are nearly ellipsoidal when viewed from

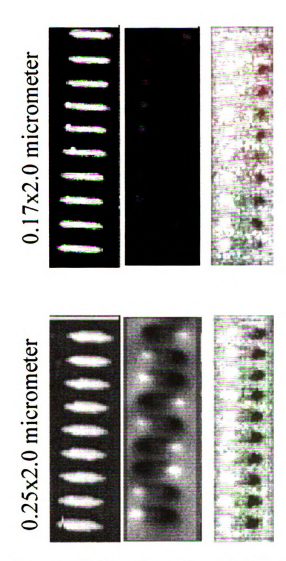


Figure 4.6: Example of how application of an external field can switch the magnetization of a finger. The top most image in each column is a topographic scan of two different width fingers. The second row shows the corresponding MFM image of the virgin state magnetization. The third row shows MFM images of the same fingers after application of an 800 Gauss field parallel to the long axis of the fingers, and directed upward on the page. Note that all magnetic images are acquired at zero applied field.

	$0.25 \mu \mathrm{m}$ width	$0.17 \mu \mathrm{m}$ width
c/b	0.060	.088
$4\pi M_{\overline{b}}^{\underline{c}}$ (Gauss)	1130	1658
H_c measured (Gauss)	400	600

Table 4.1: Comparison of Stoner-Wohlfarth Prediction to Switching Results.

above. However when viewed from the side, they will be quite sharp. Moreover, physical imperfections at edges further deviate our sample geometry from the ellipsoidal ideal, and could lower the switching field.

Figure 4.9 shows the length dependence of the switching field. Here the dependence of switching field on length is non-monotonic. This subtlety isn't readily accounted for in our simple Stoner-Wohlfarth picture.

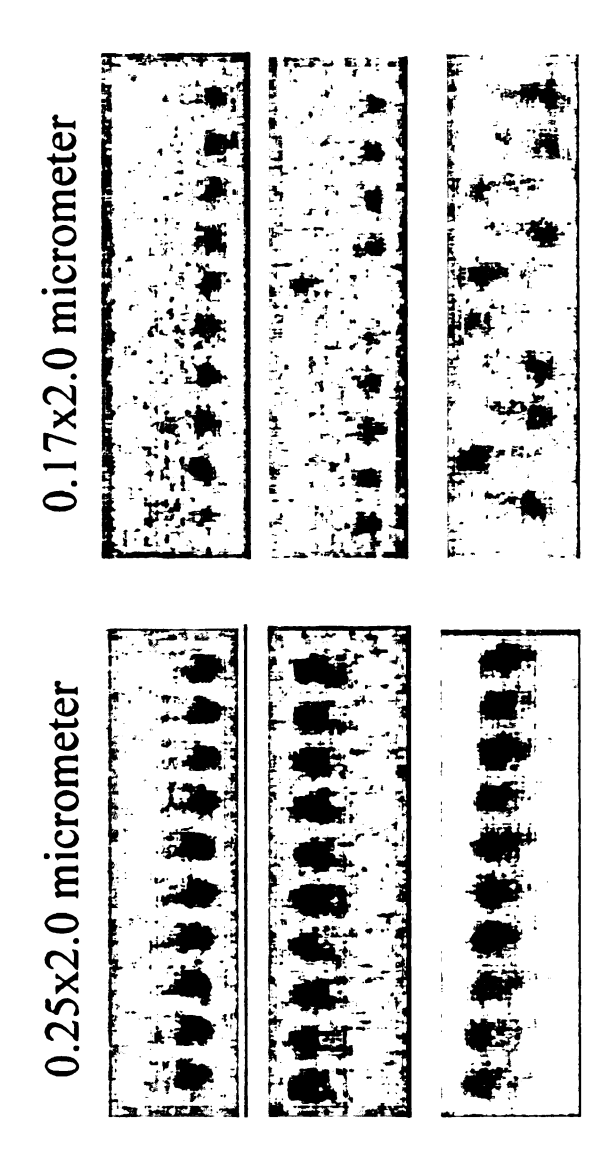


Figure 4.7: Example of the determination of the switching field. The top most image in each column shows MFM images of the same fingers from Figure 4.6 after application of an 800 Gauss field parallel to the long axis of the fingers, and directed upward on the page. The second row of pictures shows the same fingers after application of an external magnetic field of 440 Gauss directed downward on the page. The third row shows the same fingers after the field has been increased to 570 Gauss. Note that all magnetic images are acquired at zero applied field.

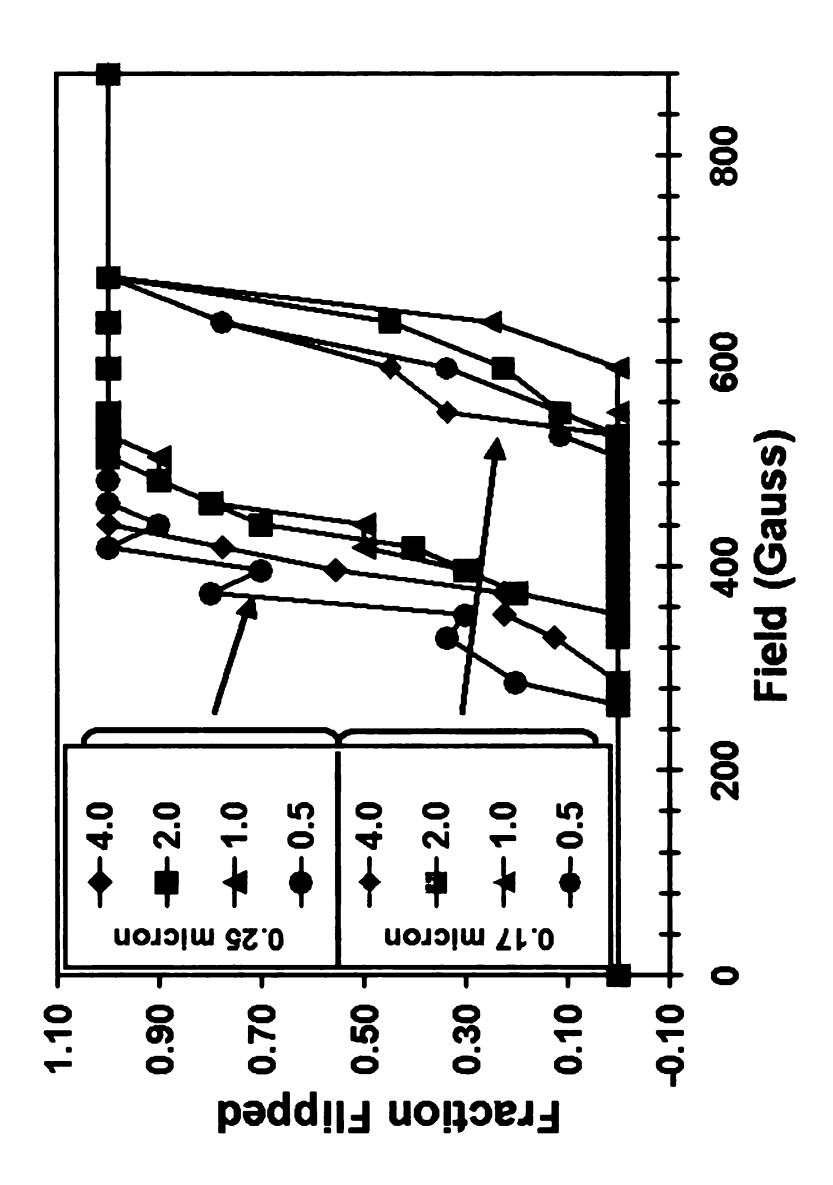


Figure 4.8: Plot showing the results of the switching experiment. The vertical axis represents the fraction of fingers of a given size that have switched their remnant state magnetization. The horizontal axis represents the applied external field. Notice that the two sets of widths separate themselves into two distinct groups having different switching fields.

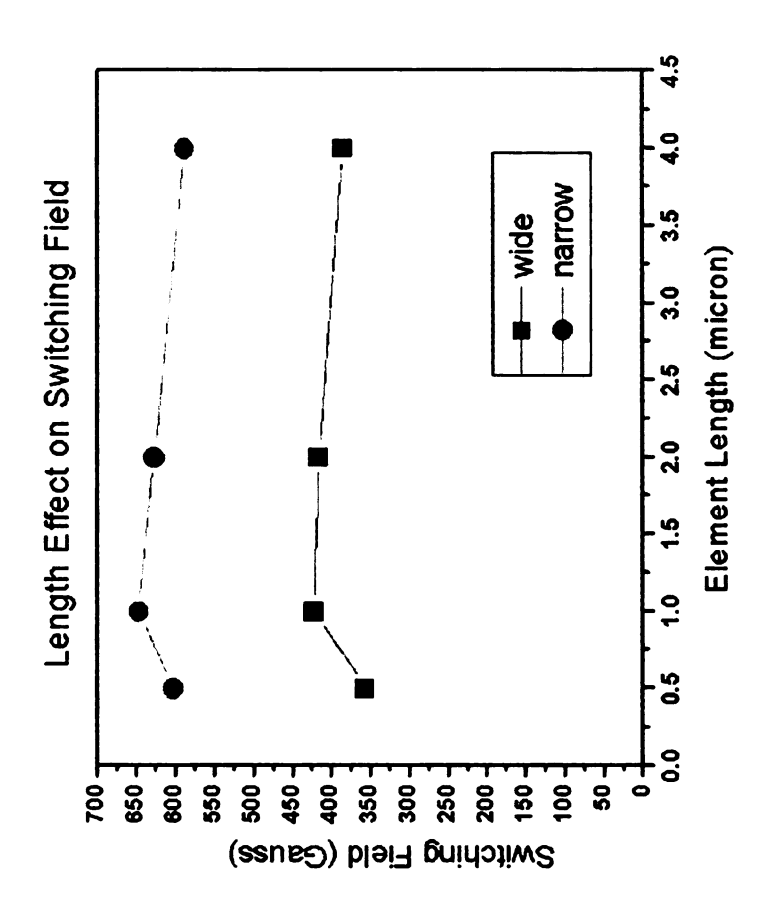


Figure 4.9: Plot showing the results of the switching experiment. Again notice that the two sets of widths separate themselves into two distinct groups having different switching fields. The length dependence, however, is nonmonotonic.

Chapter 5: Spin-Polarized

Transport: Background and

Theory

The study of spin-related electronic transport in solids dates back several decades. In 1970, Tedrow, Meservey, and Fulde performed tunneling experiments to study the Zeeman splitting of the quasiparticle density of states in a superconductor[50]. Tedrow and Meservey followed that by using the spin-split density of states as a tool to study the spin-polarization in ferromagnetic metals[51].

Direct injection (as opposed to tunneling) of spin from a ferromagnet into a nonmagnetic metal was pioneered by Johnson and Silsbee in 1985. Their sample was a macroscopic slab of pure aluminum, with two long and narrow films of permalloy evaporated on top to form the spin injector and detector. The current passed from the injector into the aluminum slab and exited at the end opposite of the slab from the detector, eliminating any IR voltage drop between injector and detector. A net spin accumulation was present at the detector due to diffusion of the nonequilibrium spin distribution from the injector to the detector. In addition to the direct detection of spin accumulation, these authors measured the Hanle effect, which is the rotation of the net spin in the presence of a magnetic field perpendicular to the direction of the injected magnetization.

Later Johnson adapted the spin accumulation experiment to a thin-film geometry, with injector and detector placed on opposite sides of the film[52, 53]. The interpretation of that experiment was questioned later by Fert and Lee[54], who claim that the Johnson data require an abnormally large spin diffusion length.

Theoretical frameworks to discuss spin accumulation were developed both by Johnson and Silsbee[55, 56] and by van Son, van Kempen, and Wyder[57, 58]. The latter treat the space-dependent chemical potentials of spin-up and spin-down electrons near interfaces between ferromagnetic and nonmagnetic metals. Those macroscopic approaches were later validated by Valet and Fert[59], who showed that the macroscopic approaches work as long as the mean free path is much shorter than the spin diffusion (or spin memory loss) length. In this chapter we will discuss a simplified approach to spin-polarized transport, which deals only with spin-dependent electrical resistances.

The main focus in the field of spin-polarized transport shifted suddenly in 1988 with the discovery of giant magnetoresistance (GMR) in Fe/Cr multilayers[60, 61]. At a certain Cr thickness, the magnetizations in nearest-neighbor Fe layers are coupled antiferromagnetically, resulting in a high resistance of the multilayer. In the presence of an external magnetic field parallel to the plane of the layers, the Fe magnetizations are brought into alignment, causing the resistance to decrease dramatically. As mentioned in the Introduction, GMR has attracted much attention due to its strong technological applications. As the field has evolved, most of the work is performed on "spin valves" rather than multilayers. A spin valve consists of only two ferromagnetic (F) layers separated by a nonmagnetic (N) layer thick enough to avoid any magnetic coupling between the F layers. One of the F layers has its magnetization pinned, usually by proximity to an antiferromagnet, while the other F layer is free to rotate in the external field.

5.1 GMR Quickly

A crude understanding of GMR can be obtained from the model shown in Figure 5.1 and Figure 5.2. The underlying assumption is that the scattering rate of

a conduction electron within the F layer, and perhaps also at the F/N interface, depends on the relative orientation of the electron's intrinsic spin and the magnetization of the material. Let us assume for argument that the scattering rate is low for the spin parallel to M, and high for the spin antiparallel to M. In each figure the balls with arrows represent electrons with either $S_z = +\frac{1}{2}\hbar$ (arrow pointing up) or $S_z = -\frac{1}{2}\hbar$ (arrow pointing down). These will furthermore be referred to as spin-up and spin-down electrons, respectively. Also in each picture are regions of alternating shades of grey, which are labelled as either an F (ferromagnetic) or a N (normal) metal. Also, each F layer is labelled with M (magnetization) and an up arrow or a down arrow. These indicate the direction of magnetization in the F layer. The long, horizontal arrows indicate fictitious independent current paths for the electrons of different spin. In Figure 5.1 the spin-up arrow and corresponding horizontal arrow, representing the spin-up current channel, passes from left to right through the multi-layer without any scattering events, which would be represented as a bend in the line. The spin-down channel, conversely, will experience a scattering event in each of the F layers. According to this cartoon, then, when the spin direction of a transport electron is anti-aligned to the direction of magnetization in an F layer, it will experience a scattering event. These scattering events will serve to increase the resistance of the spin channel. In Figure 5.2, the F layers are antiparallel, and therefore each spin channel will be anti-aligned to one layer. Consequently, each spin channel will experience a cartoon scattering event as it traverses the multi-layer, and each will pick up an additional resistance. Recall that in the parallel addition of resistances, two identical resistances in parallel give a total resistance of one-half of the individual resistances. Furthermore, if a large resistance is added to a much smaller one, then the total resistance favors the lesser. The consequence for our cartoon depiction of GMR is that in the case where the F layers are parallel (Figure 5.1) because there is a spin channel that experiences no

scattering events, the current will favor that channel, yielding a net lower resistance than the case where both channels are experiencing scattering events (Figure 5.2).

5.2 Two-Current Series-Resister Model

The two-current series-resister model approaches the GMR problem by adding up the macroscopic forms for interface and volume resistances for each spin channel independently, then making the parallel combination of the two [62]. The case to be analyzed here is depicted by the cartoon in Figure 5.3 and is analogous to the cartoons depicted in Figures 5.1 and 5.2. The ellipses represent F nanoelements similar to those of Chapter 2, and represent the F layers in the GMR cartoons. The long rectangular box in Figure 5.3 represents an N wire which crosses on top of the F elements, which is the analog of the N layer in the GMR cartoons. The line with arrows that curves from the left ellipse into the box and out the other ellipse in the sample cartoon represents a fictitious current path through the sample. With this geometry, the experiment becomes a four terminal measurement with the current leads being the portion of the F elements where the current is flowing, and the voltage leads being the portion of the F fingers where the current is not flowing. This is perhaps a crude approximation, as the current flow in such a complicated geometry will be quite non-uniform. However, to improve the accuracy of this estimate, a finite element analysis of the sample geometry would be necessary. For the time being, it will be adequate to continue with the above description.

In the four terminal picture, the voltage measured is between points lying within F near the interface between F and N. So the resistance that an electron experiences will come from the interface resistances between F and N, and the volume resistance in N. The interface resistances depend on the relative orientation of the electron spin and the direction of M in F. So the case of the F fingers parallel

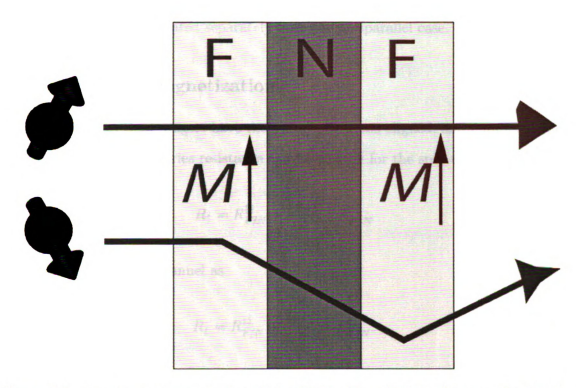


Figure 5.1: A cartoon representation of the GMR effect. This is the case of aligned F layers, which yields a lower resistance than the anti-parallel case.

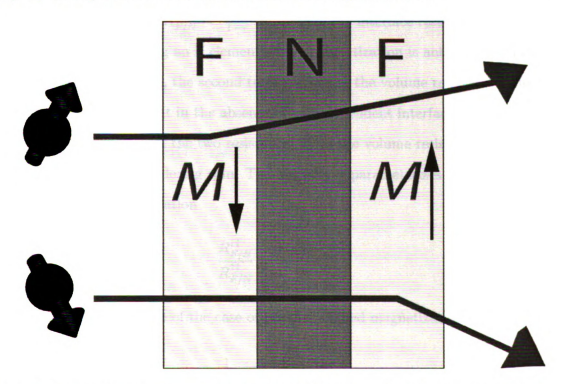


Figure 5.2: A cartoon representation of the GMR effect. This is the case of antialigned F layers, which yields a higher resistance than the parallel case.

magnetization will be treated separately from the antiparallel case.

5.2.1 Parallel Magnetizations

Assume that the F fingers have their magnetizations aligned, and parallel to the spin up direction. The series resistance can be written for the spin up channel as

$$R_{\uparrow} = R_{F/N}^{\uparrow\uparrow} + \frac{2\rho_N t}{A} + R_{F/N}^{\uparrow\uparrow} \tag{5.1}$$

and for the spin down channel as

$$R_{\downarrow} = R_{F/N}^{\downarrow\downarrow} + \frac{2\rho_N t}{A} + R_{F/N}^{\downarrow\downarrow}. \tag{5.2}$$

In all discussion to follow, $R_{F/N}^{\uparrow\uparrow}=\frac{2R_{F/N}}{1+\gamma}$ represents the interface resistance of an electron entering or leaving an F element whose magnetization is parallel to the electron spin. Conversely, $R_{F/N}^{\downarrow\downarrow}=\frac{2R_{F/N}}{1-\gamma}$ represents the interface resistance of an electron entering or leaving an F element whose magnetization is antiparallel to the electron spin. In each case, the second term represents the volume resistance. The factor of 2 is chosen so that in the absence of spin-dependent interface resistance, the parallel combination of the two resistances gives the volume resistance in the normal wire without considering spin. The quantity γ parameterizes the F/N interface and obeys the relation

$$\frac{R_{F/N}^{\dagger\dagger}}{R_{F/N}^{\dagger\dagger}} = \frac{1+\gamma}{1-\gamma}.\tag{5.3}$$

The parallel resistance of the case of parallel aligned magnetizations will be

$$\frac{1}{R_{\uparrow\uparrow,total}} = \frac{1}{R_{\uparrow}} + \frac{1}{R_{\downarrow}} \tag{5.4}$$

which yields

$$\frac{1}{R_{\uparrow\uparrow,total}} = \frac{1}{2R_{F/N}^{\uparrow\uparrow} + 2\frac{\rho_N t}{A}} + \frac{1}{2R_{F/N}^{\downarrow\downarrow} + 2\frac{\rho_N t}{A}}$$
 (5.5)

which yields

$$R_{\uparrow\uparrow,total} = \frac{(R_{F/N}^{\uparrow\uparrow} + \frac{\rho_N t}{A})(R_{F/N}^{\downarrow\downarrow} + \frac{\rho_N t}{A})}{(\frac{R_{F/N}^{\uparrow\uparrow} + R_{F/N}^{\downarrow\downarrow}}{2}) + \frac{\rho_N t}{A}}.$$
 (5.6)

5.2.2 Antiparallel Magnetizations

Similarly, we may write for the antiparallel case for the spin up channel

$$R_{\uparrow} = R_{F/N}^{\uparrow \uparrow} + \frac{2\rho_N t}{A} + R_{F/N}^{\downarrow \downarrow} \tag{5.7}$$

and for the spin down channel as

$$R_{\downarrow} = R_{F/N}^{\downarrow\downarrow} + \frac{2\rho_N t}{A} + R_{F/N}^{\uparrow\uparrow}. \tag{5.8}$$

Which leads to a total resistance of

$$R_{\downarrow\downarrow,total} = \frac{R_{F/N}^{\uparrow\uparrow} + R_{F/N}^{\downarrow\downarrow}}{2} + \frac{\rho_N t}{A}.$$
 (5.9)

5.2.3 Calculating the GMR Signal

The GMR signal measured will be related to the difference between the resistance of the parallel and antiparallel magnetization states. Notice that no assumption has been made a priori regarding the relative sizes of the interface resistances, only that the resistance is determined by whether the electron spin is aligned or anti-aligned to the magnetization at the interface. That is to say, there is no distinction made in this case between an up electron entering a down magnetization layer or a down electron entering an up magnetization layer. So, the

quantity to look to is

$$\Delta R = R_{11,total} - R_{\uparrow\uparrow,total}. \tag{5.10}$$

Substituting Equation 5.6 and Equation 5.9 into Equation 5.10 gives

$$\Delta R = \frac{R_{F/N}^{\uparrow\uparrow} + R_{F/N}^{\downarrow\downarrow}}{2} + \frac{\rho_N t}{A} - \frac{\left(R_{F/N}^{\uparrow\uparrow} + \frac{\rho_N t}{A}\right) \left(R_{F/N}^{\downarrow\downarrow} + \frac{\rho_N t}{A}\right)}{\left(\frac{R_{F/N}^{\uparrow\uparrow} + R_{F/N}^{\downarrow\downarrow}}{2}\right) + \frac{\rho_N t}{A}}.$$
 (5.11)

Simplification yields

$$\Delta R = \frac{1}{4} \frac{(R_{F/N}^{\uparrow \uparrow} - R_{F/N}^{\downarrow \downarrow})^2}{\frac{R_{F/N}^{\uparrow \uparrow} + R_{F/N}^{\downarrow \downarrow}}{2} + \frac{\rho_N t}{4}}.$$
 (5.12)

This may be rewritten as

$$\Delta R = \frac{\frac{(R_{F/N}^{\dagger\dagger} + R_{F/N}^{\dagger\dagger})^2}{4} \frac{(R_{F/N}^{\dagger\dagger} - R_{F/N}^{\dagger\dagger})^2}{(R_{F/N}^{\dagger\dagger} + R_{F/N}^{\dagger\dagger})^2}}{\frac{R_{F/N}^{\dagger\dagger} + R_{F/N}^{\dagger\dagger}}{2} + \frac{\rho_N t}{A}}.$$
 (5.13)

Defining

$$\gamma = \frac{R_{F/N}^{\uparrow\uparrow} - R_{F/N}^{\perp}}{R_{F/N}^{\uparrow\uparrow} + R_{F/N}^{\downarrow\downarrow}} \tag{5.14}$$

and

$$R_{F/N}^* = \frac{R_{F/N}^{\uparrow \uparrow} + R_{F/N}^{\downarrow \downarrow}}{4} = \frac{R_{F/N}}{1 - \gamma^2}$$
 (5.15)

Equation 5.13 can be written as

$$\Delta R = \frac{(2\gamma R_{F/N}^*)^2}{2R_{F/N}^* + \frac{\rho_N t}{A}}.$$
 (5.16)

The form for ΔR in Equation 5.13 is positive definite, from which can be inferred that the antiparallel resistance is larger that the parallel one.

5.3 Application of ΔR

The form for Equation 5.16 would apply to a multilayer stack where the current flow is essentially uniform over the area of the sample (especially in cases where superconducting leads are used), and will have to be amended to account for cases of nonuniform current flow, such as that depicted in Figure 5.3.

Often in the literature the CPP GMR signal is given in units of $A\Delta R$, where A is the cross-sectional area of the multilayer stack, as it is a quantity that is sample independent. In this case it is trivial to recast Equation 5.16 into this form by multiplying everywhere by a factor of A such that

$$A\Delta R = \frac{(2A\gamma R_{F/N}^*)^2}{2AR_{F/N}^* + \rho_N t}.$$
 (5.17)

However in the case of nonuniform current flow, there are two areas to note. One is the interface area between F and N and the other is the cross-sectional area of the N wire. This subtlety will be discussed in greater detail in Chapter 7.

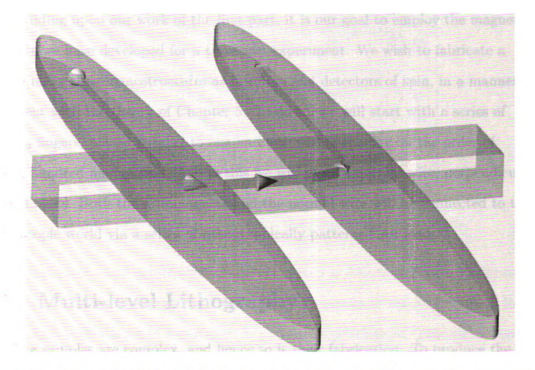


Figure 5.3: Schematic of the GMR device to be analyzed. This geometry represents a gross approximation to the devices used later in this work.

Chapter 6: Spin-Polarized

Transport: Experimental

Procedure

Building upon our work of the first part, it is our goal to employ the magnetic elements we have developed for a transport experiment. We wish to fabricate a sample using these nanostructures as injectors and detectors of spin, in a manner consistent with the theory of Chapter 5. To do so, we will start with a series of $Co_{91}Fe_{9}$ fingers, placed parallel to one another, with a spacing on the order of several hundred nanometers. Across this we will place a normal wire, perpendicular to the fingers. Both the ferromagnets and the normal wire will be connected to the macroscopic world via a series of lithographically patterned Au leads.

6.1 Multi-level Lithography

The samples are complex, and hence so is their fabrication. To produce the desired features, we must perform a series of independent lithographic steps. To start with, we make a set of large leads to which we will later connect wires to the outside world. These leads are fabricated using photolithography.

6.1.1 Photolithography

Photolithography (PL) is a technique which is almost identical to EBL, but which uses ultraviolet light to expose the polymer resist, rather than a focused electron beam. A typical PL process is listed in Table 6.1. Notice that the sequence

of steps follows in parallel with that for EBL listed in Table 3.1. The difference here is that in order to produce our undercut, we don't employ a bi-layer. It is possible to accomplish the undercut using a bi-layer by first spinning a layer of resist, administering a blanket exposure of the entire layer, then spinning the top layer. But for this experiment, we have employed a technique of soaking a single layer of resist in Chlorobenzene. This serves to 'harden' the top portion of the resist layer, making it develop more slowly and hence producing the desired undercut.

Spin	Shiplee S1805	4000 rpm	40s
Bake		95°C	30min
Cool			
Expose	AB-M Mask Aligner		2.3sec
Soak	Chlorobenzene	30°C	20S
Bake			5min
Develop	Microposit 452	23°C	45S
Rinse	DI		20S
Metalize			
Liftoff	Acetone	60°C	1hour

Table 6.1: Recipe used to produce the photolithographic leads.

The pattern to be printed by the exposure step is determined by a mechanical mask. This is made from a piece of glass, typically quartz or soda-lime, which has been coated with a layer of metal such as chrome or germanium. This metal layer will be processed away, typically via a lithography of its own, to leave the mask transparent in regions to be exposed. These masks are best purchased commercially, and can be obtained by supplying the desired pattern in a computer drafting file to the manufacturer. The file used to produce the mask for these leads is shown in Figure 6.1. The overall size of the print area is 0.5inch on a side. The actual bonding pads are 1.0mm on a side. Figure 6.2 shows a zoom of the area in which we will write the sample using EBL. The vertical distance available for writing is $40\mu m$ and the horizontal is $60\mu m$. In Figure 6.1 are visible the short wires which connect each of the contact pads. These are to prevent damage to the sample during handling.

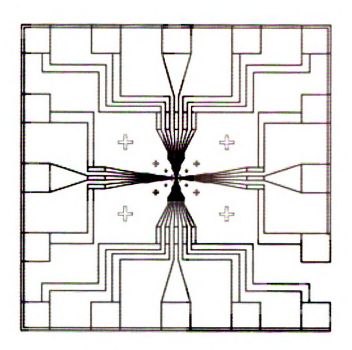


Figure 6.1: An overview of the photomask used to to produce the photolithographic leads to which current and voltage leads may be attached later.

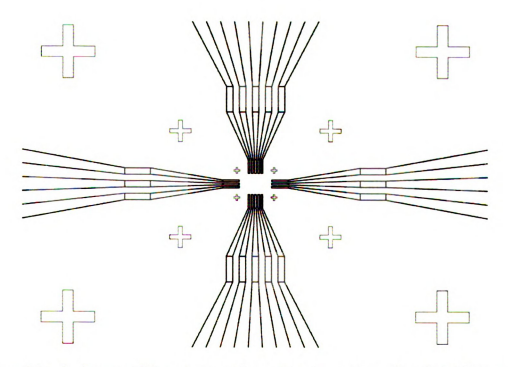


Figure 6.2: A closeup of the photomask used to to produce the photolithographic leads to which current and voltage leads may be attached later.

These are then scratched to disconnect the pads just prior to measurement.

6.1.2 Alignment

The real trick to achieving multi-level lithography is ensuring that the features you produce in the various steps are aligned. In order to align the EBL steps with the optical, there are a series of crosses placed in the photolithographic lead pattern. These are visible in Figure 6.1 and again in Figure 6.2. These marks are placed for several different magnifications of the EBL system. In this way, alignment may be preformed step-wise, first aligning at low resolution, then increasing the resolution and realigning. The computer software which controls the EBL system is designed to accommodate such alignment. The size, shape and position of the alignment marks that have been printed previously in the photolithographic step are supplied to the software, as well as the area that will form windows around the mark. After loading a set of Au leads into the EBL system, the alignment program is invoked. What is presented to the user is a set of windows, each of which contains an outline of a virtual alignment mark, as well as a live scan of the area of the alignment mark. The user may then move the virtual mark about until it aligns with actual mark. Once they are aligned, the software computes a matrix which contains information about the displacement and rotation of the sample relative to the EBL system. Such alignment is necessary because each time a sample is loaded, the position and orientation of the sample will be different. The alignment process provides a way to register the position and orientation of the sample for each lithography. Table 6.2 lists steps involved in the process. Proceeding in this way, alignment to within an accuracy of better than 100nm in successive EBL steps has been performed.

Table 6.2: Step-by-step description of the EBL alignment technique.

- Start with sample prepared with Au photolithographic leads
- Spin EBL resist layer as per process
- Load into EBL system (JOEL JSM 840 SEM)
- Focus/Stigmate at high resolution
- At 200X, center substrate roughly
- blank beam, switch to external raster control
- launch graphical interface program for EBL
- invoke the alignment program from the graphical interface
- use arrows keys on computer keyboard to align virtual marks with life scan
- press space to calculate intermediate matrix
- repeat arrow key/space bar to ensure good alignment
- press enter to save matrix
- increase magnification to 800X
- continue alignment, using arrows/space bar, to align 800X virtual and actual marks
- save matrix
- quit alignment
- select write 'with alignment' from the graphical interface
- write the appropriate sample pattern

Base Pressure	3×10^{-6} Torr	
Milling Pressure	$3 \times 10^{-4} \text{Torr}$	
Flow Rate	6 SCCM	
Current	20mA	
Voltage	500V	

Table 6.3: Typical ion mill parameters for Au milling.

6.2 Ion Milling

An important part of this fabrication technique is the use of a short ion-mill just prior to deposition of the normal metal. Ion milling is a momentum transfer process whereby atoms or molecules from a sample are removed by the bombardment of the surface with ions, hence the name. In our samples the ion milling removes the Au protecting layer from the ferromagnetic elements in the area where the normal metal will be placed (the patterned resist layer protects the remaining features from the ion mill beam). We do so to ensure ohmic metal-to-metal contact between the ferromagnetic and normal metals. In other experiments of this nature, the ion mill has also been used to remove the native oxide layer that forms on unprotected ferromagnetic elements [63]. Typical ion milling parameters for Au milling are listed in Table 6.3. These parameters yield a sputter rate of $38.5 \frac{nm}{min}$

6.3 The Quick Dipper

For the purposes of measuring these samples, a "quick dipper" system designed and built by Prof. William P. Pratt, Jr. is utilized. The quick dipper consists of a large mouth He dewar into which is inserted a sample probe. The probe has an electronics and plumbing connections package at the top of a long skinny tube, with superconducting solenoid magnet at the bottom. Samples are mounted onto a stage, and wires are bonded to the samples leads using Ag conducting paint. The wires then attach to a Bishop Graphics strip consisting of 6 Cu stripes on a

non-conducting backing. These wires are bonded to the Cu stripes using Rose's Alloy solder. The other end of the Cu strips attach to wire that travel through the tube to the electronics package at the top. These connections to the Cu are made using standard resin core solder. The reason for differing solders is that the melting points are different. The standard solder connections are made first, then those using the Rose's Alloy. Because the Rose's Alloy possess a lower melting point, the first solder connections won't be affected. Figure 6.3 shows a schematic representation of the quick dipper sample area, including the sample $(\frac{1}{2}$ inch on a side), and the bishop graphics connectors for wire bonding. Over this entire assembly is placed a brass cap which slides up from the bottom and completely covers the sample area. The entire assembly then slides into a second tube containing the superconducting magnet, and both tubes are lowered together into the He dewar. To warm up and load a new sample, only the inner tube need be removed. The outer tube containing the magnet need not be removed at this point.

This system design greatly improves sample throughput. Samples may be run and switched quickly, with very little warm up/cool down time.

6.4 Sample Mounting

Sample mounting is a subject of great concern. The samples involved in this work have extremely small cross-sectional areas. Even a minute transient voltage will produce exceedingly high current densities in the sample region. It is therefore necessary to take great precaution in the mounting of the sample. The first and most important thing is to make sure that everything that the sample will come into contact with is grounded. A grounding strap from the body of the quick dipper to a suitable place, such as the screened room into which the measurement system is moved, which is itself grounded to the building transformer is recommended.

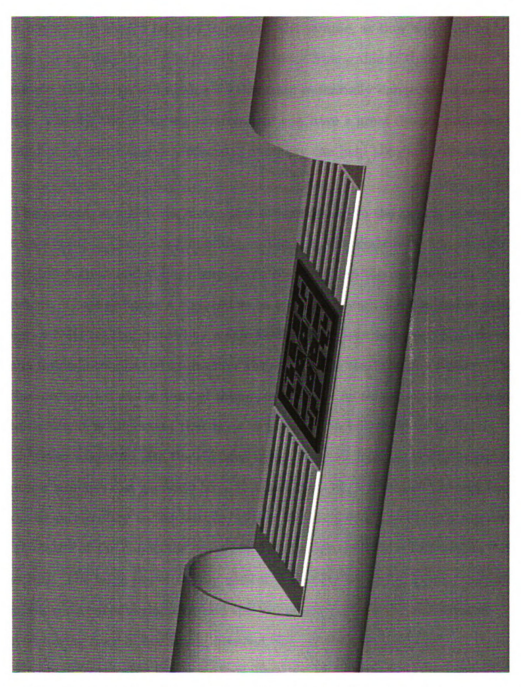


Figure 6.3: A schematic representation of the quick dipper apparatus used to measure the samples in this experiment.

Anyone involved in the sample mounting procedure should also be grounded at all times. Wrist straps are readily available for this purpose. Moreover, nothing which is non-conducting should be used to contact the sample, as they will tend to build up static charge and their voltage will float away from ground. Upon contact with the sample, the charge will dissipate generating potentially dangerous transient voltages. Finally, the mounting environment can have a great deal of influence on the build up of static charge. Adequate humidity can help alleviate such static build up.

The manner in which the electronics are connected to the sample is also of great importance. There are grounding switches on the electronics box used to connect the current and voltage leads from the dipper to the measurement equipment. These switches are placed so as to connect each sample lead to ground through a $1M\Omega$ resister, providing a safe path for spurious voltages. The connection is made immediately as the leads enter the electronics box from the dipper. The switches are opened at the time of the measurement. As the electronics are added to the circuit, it is important that they be powered on before bringing the dipper/dewer assembly into the shielded room. At start up, large draw equipment like power supplies can generate large line voltages that can couple through the measurement circuitry to the sample. When connections are made, it is important that the leads of the connector are grounded through the user to the dipper before connecting. The large power supply used to power the superconducting magnet should have its outputs shunted, and the low output grounded. The shunt is removed during normal operation, however the ground remains intact.

Finally, it is possible to use various filters for the protection of the sample. For instance, a simple RC filter on each lead consisting of a resistor in series with the sample coupled with a capacitor to ground will act as a low pass filter, discouraging high frequency transients from travelling down the leads to the sample.

Following these simple techniques cannot guarantee a successful mounting, though they will greatly reduce the risk of catastrophic failure.

6.5 Low Noise Measurement Circuit and Techniques

Measurement of low-level voltages requires specialized techniques for amplification and elimination of noise. The basic circuit used is depicted in Figure 6.4. A Stanford Research Systems (SRS) DS345 Synthesized Function Generator is used to excite the sample. In series with the sample is a ballast resistor whose resistance is much greater than that of the sample. The combination of function generator and ballast resister appear as a current source to the sample, which is supplying

$$I_{source} = \frac{2 \times V_{rms,DS345}}{R_{bollost}}. (6.1)$$

The factor of 2 in the above is an artifact of a mismatched impedance at the output of the SRS function generator.

The voltage is measured in a four-terminal configuration to eliminate lead resistances from the measurement. There is no current flow in the voltage leads, and therefore no IR (current times resistence) drop. The voltage leads head into a SRS Model SR552 Bipolar Pre-amplifier. The output of the preamp becomes one input of a lock-in amplifier. The other is the output of a Singer Gertsch Ratio Transformer. The lock-in used is an SRS Model SR530. The two inputs are subtracted, and the ratio transformer is tuned to null out the background resistance of the sample. By doing so, the dynamic range of the lock-in is available to measure the change in sample resistance.

The output of the lock-in is passed into a Keithley DMM, which is under

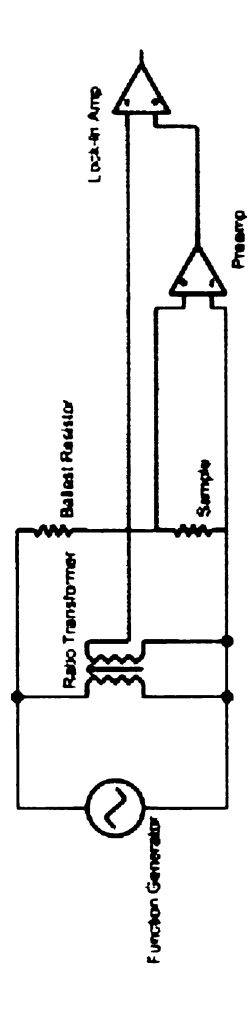


Figure 6.4: Diagram of the circuit used to measure the samples in the transport experiment.

control from a personal computer via a GPIB interface. The software for the experiment is written in Labview.

Chapter 7: Spin-Polarized

Transport: Experimental Results

To begin, a sample is mounted into the quick dipper. After mounting, it is inserted into the He dewar. All measurements are made at liquid He temperature (4.2K). Drive is applied to the sample, and the four-terminal resistance is measured. Next the ratio-transformer is introduced, and the A-B signal is nulled by adjusting the ratio. After nulling, the four-terminal resistance of the sample is measured as a function of the applied magnetic field. In each case a large field was first applied in the plane of and parallel to the long axis of the fingers. This field defines the positive direction. This large field ensures that the magnetizations in the fingers are parallel. The field is then returned to zero, and increased gradually in the negative direction until first one, and then both fingers reverse their magnetization. The field is returned again to zero, and then increased gradually in the positive direction. Measurements are made in-situ with the field, which is held constant during the measurement.

Of the many samples produced and measured in this experiment, many had problems with contacts between the normal and ferromagnetic metals. Data from the two best samples are presented here. The first sample which is shown in figure 7.1 is an additively patterned set of 15 nm thick gold-capped $Co_{91}Fe_{9}$ fingers crossed by a 30nm thick Ag wire. The four-terminal resistance measured between the pair of adjacent F fingers labeled in Figure 7.1 was 1.2 Ω .

The data presented represent a typical graph in which run parameters have been optimized for best signal-to-noise ratio. The run parameters for this run are summarized in Table 7.1. In all experiments, however, different drive currents were

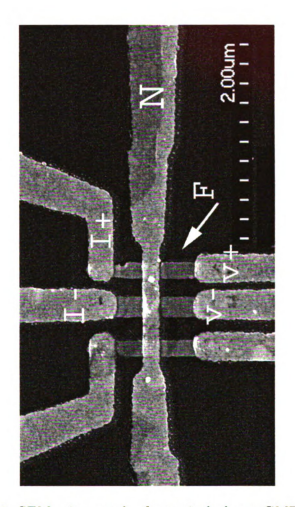


Figure 7.1: SEM micrograph of a typical planar GMR sample.

tried. It was not possible, however, to increase drive current indefinitely as there is fear of either destroying the sample or heating it excessively.

Drive Amplitude	$2.5V_{rms}$ (X2)
Drive Frequency	100Hz
Ballast Resister	100ΚΩ
Drive Current	$50\mu\mathrm{A}$
Ratio	0.00117
PreAmp Gain	100
Lock-In Sensitivity	$20\mu V$
Lock-In Phase Shift	18.3°
Lock-In Band Pass Filter	In
Lock-In Line Filter	In

Table 7.1: Measurement parameters used in acquisition of data in Figure 7.2.

Figure 7.2 shows that the magnetoresistance of this sample displays a clear spin-valve signal, with discrete jumps corresponding to magnetization reversal in specific F fingers. As the field is increased in the negative direction, the wide finger flips anti-parallel to the narrow one at a field of approximately -1000 Oe. This gives rise to the higher resistance magnetic state. At a field of approximately -1300 Oe the resistance drops as the narrower finger switches and the fingers are again parallel. This is repeated in the positive field direction. There are two curiosities to note, one is that while the switching fields are symmetric, the MR response is greater in the negative field direction than in the positive, possibly due to an additional small magnetic domain that a subsequent MFM image has revealed. However, this explanation also would require a non-zero MR in our data at fields below -1300 Oe, which does not appear to be the case. Also of interest is the narrow negative MR response that occurs just before the larger, positive one. We do not currently have an explanation for this feature.

The second sample is a subtractively patterned set of Co₉₁Fe₉ fingers crossed by a 30nm thick Cu wire. The subtractive patterning is achieved by first depositing a thin film, patterning the fingers, putting down a mask metal, and lifting off the

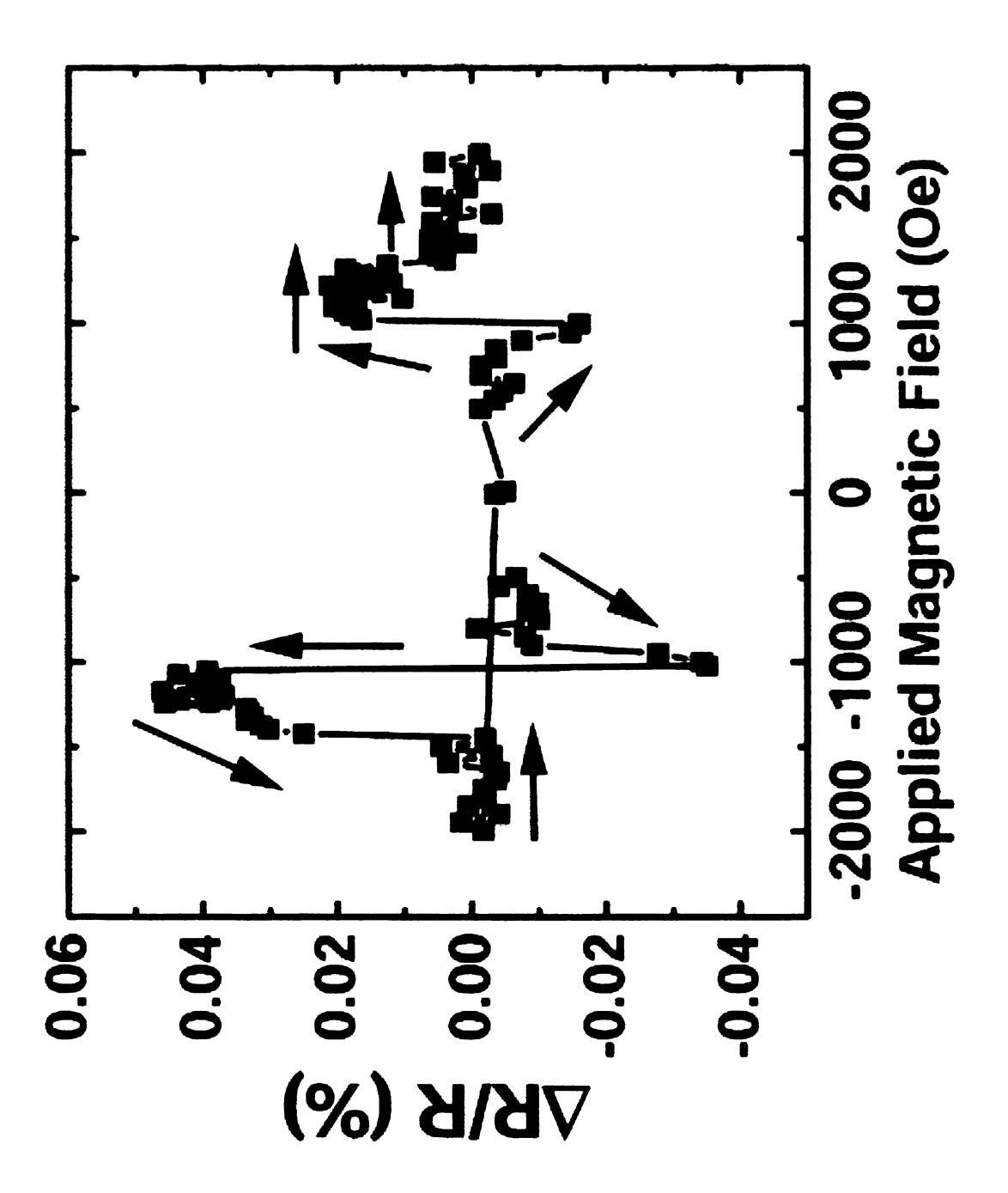


Figure 7.2: The GMR response of a planar F/N/F structure. This sample was additively patterned $Co_{91}Fe_9$ with a Ag wire.

resist. The mask metal is left only in the regions of the desired fingers. At this point the sample is ion milled to remove the unwanted thin film material, leaving just the fingers. As a final step the remaining mask material may be wet etched, unless the ion mill time was large enough to completely remove the mask.

The 4-terminal resistance between adjacent fingers for this sample was 1.7Ω . The run parameters are summarized in Table 7.2 Here the situation is less well defined. Our MFM studies indicate that there may be a non-uniform magnetization within the fingers, which is probably an artifact of the ion-mill patterning. The ion-mill process introduces atomic disorder, which in turn influences the magnetic structure. As the data show in Figure 7.3, there isn't a well defined transition from parallel to anti-parallel. Moreover, there is some additional structure to the field dependence of the resistance that isn't explained by the simple parallel/anti-parallel model. Nevertheless, the relative size of the MR signal is similar to that of the first sample shown in Figure 7.2.

Drive Amplitude	$0.2V_{rms}$ (X2)
Ballast Resister	10ΚΩ
Drive Frequency	100Hz
Drive Current	$40\mu\mathrm{A}$
Ratio	0.01774
PreAmp Gain	100
Lock-In Sensitivity	$50\mu V$
Lock-In Phase Shift	22.4°
Lock-In Band Pass Filter	In
Lock-In Line Filter	In

Table 7.2: Measurement parameters used in acquisition of data in Figure 7.3.

In order to estimate whether the size of the measured GMR signal for the data shown in Figure 7.2 is reasonable, it is possible to use Equation 5.17 with some amendment. Although parameters for the $Co_{91}Fe_{9}/Ag$ interface in our experiment have not been measured, they are probably similar to the $Co_{91}Fe_{9}/Cu$ interface, for which $\gamma = 0.75$ and $AR^*_{CoFe/Cu} = 0.52$ f Ω m² [64]. With regard to the area problem,

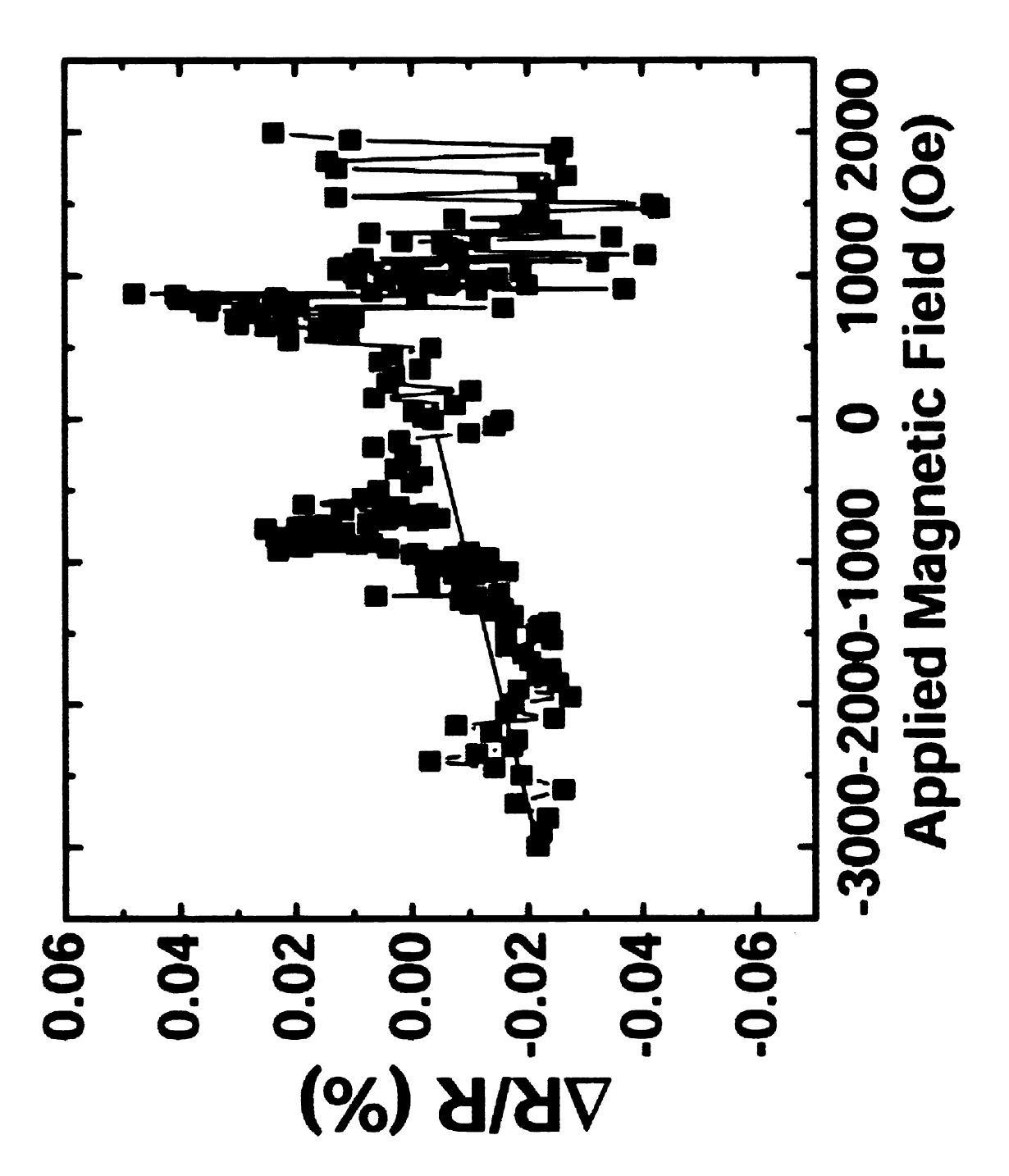


Figure 7.3: The GMR response of a planar F/N/F structure. This sample was subtractively patterned $Co_{91}Fe_9$ with a Ag wire.

as discussed in Section 5.3, it is necessary to ask what is meant by the area on the left hand side of Equation 5.17. In the case of multilayers where the current is passed perpendicular to the planes, it is natural that the area would be the cross-sectional area of the stack, as that is the area of the region active in current transport. In our geometry, however, the F/N contact area is greater than the cross-sectional area of the wire by about a factor of 6. It is not clear, then what the appropriate area to use here is. However, for the purposes of estimating the value of ΔR , we may use a range of areas bounded by the wire cross section on one end and the total F/N contact area on the other. Using those values of the area, as well as for this sample $t_N = 200$ nm (the approximate distance between adjacent fingers) and $\rho_N = 25~\Omega$ nm (obtained using the wire dimensions and the four-terminal resistance of 1.2Ω), we obtain $6 \times 10^{-4}~\Omega \leq \Delta R \leq 2 \times 10^{-2}~\Omega$, or $6 \times 10^{-4}~\leq \frac{\Delta R}{R} \leq 2 \times 10^{-2}$.

That our value falls just outside the low end of the estimate may indicate the presence of spin memory loss mechanisms not included in Equation 5.17, either at the F/N interface or in the N wire. Estimates of the spin-orbit scattering length from weak localization measurements in Ag wires similar to those used here are about 500 nm[65], long enough not to cause significant spin memory loss on the scale of this experiment. Further measurements as a function of the distance between the F injector and detector fingers will be required to sort this out.

Additionally, it has become a question what effect the Au capping layer has on the measured GMR signal. It is possible that Au forms a short circuit connecting the current leads to the N wire. Given that the resistivity of Au at low temperatures is several times smaller than that of $\text{Co}_{91}\text{Fe}_9$ ($\rho_{Au}=5n\Omega m[5]$, $\rho_{CoFe}=70n\Omega m[64]$) means that a significant portion of the current is passing in through the gold and in parallel with F. The result might be a reduced spin polarization entering the N wire, and hence a lower GMR. One solution to this problem is to eliminate the Au protecting layer, though it isn't clear what effect the

oxidation of the Co₉₁Fe₉ would have on the magnetic properties of the sample. In that case, a different choice of F might be necessary. Jedema et. al have measured a similar effect in unprotected permalloy/Cu structures[63], and obtained spin-dependent signals substantially larger than ours. Using permalloy without protection could provide a starting point for testing this idea.

Chapter 8: Conclusions

This work lays out the ground work for a new type of spin-transport experiment. By designing a new type of spin injector and detector that utilizes carefully crafted single-domain ferromagnetic particles, we have opened up a plethora of new experiments that probe spin-transport phenomena on the micron length scale. This is accomplished by moving away from multi-layers into a planar geometry. The multi-layers certainly provide a more simple case to study analytically, but the planar geometry allows greater flexibility in experiment design, as well as the increased length scale.

Though the primary thrust of this work has always been and remains spin-transport, on the way to making such a measurement a myriad of technical and scientific issues had to be addressed. This led into a long and intellectually fruitful study of the magnetic properties of single-domain mesoscopic features. In the first part of this work has been laid out a protocol for fabricating and characterizing magnetic structures, with an emphasis on their applicability to spin-transport experiments. This includes using shape-anisotropy to control the magnetization and switching behavior of the magnetic features, as well as careful choice and processing of the material. This work has shown one possible way to employ electron beam lithographic techniques in using multiple metals deposited in separate stages, using alignment, to produce complicated structures for this purpose. This fabrication procedure, as defined in this work, is by no means trivial.

The spin-transport experiment chosen as the first attempt to test the validity of the new geometry was a GMR measurement using one injector and one detector crossed by a normal wire. This geometry has direct analogy to the CPP spin-valve multilayer structure [66, 67]. Though the signal is relatively small for these devices

 $(\frac{\Delta R}{R} = 4 \times 10^{-4})$, it is not unreasonable when compared to the two-current series resister model. The analysis of these structures is quite a bit more complicated than the case of multilayers, however, owing to the non-uniform current flow through the sample. Further work will be necessary to analyze the exact nature of the current flow, as well as adapt the transport equations to this geometry.

The possibilities for future experiments involving samples of this type are quite exciting and varied. The current sample design can be extended employing an improved design as shown in Figure 8.1. By adding more detectors along the wire, it should be possible to map the GMR signal as a function of distance from the injector. Information about the spin-relaxation length in the normal wire could be extracted therefrom. It is also desirable to extend these measurements into new metals. Though Jedema et al. [63] have measured a similar signal in permalloy and Cu structures, they have failed in other combinations for reasons not yet clear. That we have seen the signal in a different material combination is of significance. Another difference between our technique and that of Jedema et al. is that their experiment requires the fabrication of different samples for each length measured, where ours in principle will be able to measure the length dependence in a single sample. Jedema et al. reported a very long spin diffusion length in Cu at low temperature $(1\mu m)$. It is important to see if the spin-diffusion length measure by our technique is consistently longer than that measure by other techniques, or if these give commensurate results.

There are also other lead configurations available, such as letting the current leave via the normal wire, rather than through the detector, which finds analogy in the "potentiometric" technique of Johnson et al.[32]. This case is of interest because the non-equilibrium spin distribution developed by the spin-accumulation at the injector can be measured in a region away from the actual current flow. It is of interest to see if these techniques yield the same signal. There has not yet been an

experiment in which both configurations have been measured in the same sample. Moreover, there is a question as to what effect having a magnetic element present at a position between the injector and detector would have on the non-equilibrium spin-distribution.

Finally there is the possibility of incorporating tunnel junctions between the ferromagnetic and normal features, as well as incorporating superconducting elements and wires into the device.

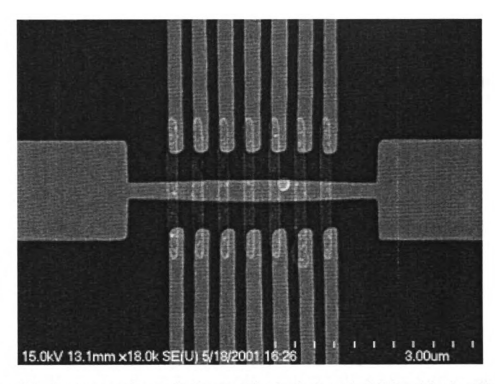


Figure 8.1: An improved sample design. The inclusion of additional leads will allow greater flexibility in designing future experiments.

List of References

- [1] A. H. Morrish, *The Physical Principles of Magnetism* (John wiley and Sons, New York, 1965).
- [2] D. R. Tilley and J. Tilley, Superconductivity and Superfluidity, 3rd ed. (Institute of Physics Publishing, Philadelphia, 1974).
- [3] J. S. Townsend, A Modern Approach to Quantum Mechanines (McGraw-Hill, New York, 1992).
- [4] J. D. Jackson, *Classical Electrodynamics*, 2nd ed. (John Wiley and Sons, New York, 1975).
- [5] N. W. Ashcroft and N. D. Mermin, *Solid State Physics* (Harcourt Brace College Publishers, Fort Worth, 1976).
- [6] W. Heisenberg, Zeits. Phys. **49**, 619 (1928).
- [7] W. Heisenberg, Zeits. Phys. 38, 411 (1926).
- [8] P. Dirac, Proc. Roy. Soc. **112A**, 661 (1926).
- [9] J. V. Vleck, The theory of Electric and Magnetic Susceptibilities (Oxford University Press, New York, 1932).
- [10] G. A. Prinz, Phys. Today **58**, 58 (1995).
- [11] K. Johnson, J. Appl. Phys. 87, 5365 (2000).
- [12] http://www.almaden.ibm.com/sst/html/leadership/leadership.htm.
- [13] D. Weller and A. Moser, IEEE Trans. Magn. 35, 4423 (1999).
- [14] S. Charap, P. Lu, and Y. He, IEEE Trans. Magn. 33, 978 (1997).
- [15] H. Bertram, H. Zhou, and R. Gustafson, IEEE Trans. Magn. 34, 1845 (1998).
- [16] K. O'Grady and H. Laidler, J. Magn. Magn. Mater. **200**, 616 (1999).
- [17] D. Thompson and J. Best, IBM J. Res. Devl 44, 2000 (2000).
- [18] E. E. Fullerton, D. Margulies, M.E.Schabes, M. Carey, B. Gurney, A. moser, and M. Doerner, Appl. Phys. Lett 77, 23 (2000).
- [19] http://www.research.ibm.com/resources/news/20010518pixiedust.shtml.
- [20] M. Hwang, M. Abraham, T. Savas, H. I. Smith, R. Ram, and C. Ross, J. Appl. Phys. 87, 5108 (2000).

- [21] K. Kirk, J. Chapman, S. McVitie, P. Aitchison, and C. Wilkinson, J. Appl. Phys. 87, 5105 (2000).
- [22] R. White, R. New, and R. Pease, IEEE Trans. Magn. 33, 990 (1997).
- [23] R. New, R. Pease, and R. White, J. Vac. Sci. Technol. B 12, 3196 (1994).
- [24] S. Chou, M. Wei, P. Krauss, and P. Fischer, J. Vac. Sci. Technol. B 12, 3695 (1994).
- [25] http://web.mit.edu/6.933/www/core.html.
- [26] S. Tehrani, J. Slaughter, E. Chen, M. Durlam, J. Shi, and M. DeHerrera, IEEE Trans. Magn. 35, 2814 (2000).
- [27] W. J. Gallagher, S. Parkin, Y. Lu, X. Bian, A. Marley, R. Altman, S. Rishton, K. Roche, C. Jahnes, T. Shaw, and G. Xiao, J. Appl. Phys 81, 3741 (1997).
- [28] R. Scheuerlein, W. J. Gallagher, S. Parkin, A. Lee, S. Ray, R. Roberazzi, and W. Reohr, IEEE ISSCC Dig. of Tech. Papers 43, 128 (2000).
- [29] M. Johnson, IEEE Spectrum 1, 33 (2000).
- [30] S. Tehrani, B. Engel, J. Slaughter, E. Chen, M. DeHerrera, M. D. P. Naji, R. Whig, J. Janesky, and J. Calder, IEEE Trans. Magn. 36, 2752 (2000).
- [31] M. Durlam, P. Haji, M. Deherrera, S. Tehrani, G. Kerszykowski, and K. Kyler, IEEE ISSCC Dig. of Tech. Papers 43, 128 (2000).
- [32] M. Johnson and R. H. Silsbee, Phys. Rev. Lett. 55, 1790 (1985).
- [33] G. Bergmann, Phys. Rep. **107**, 1 (1984).
- [34] M. Todorovic, S. Schultz, J. Wong, and A. Scherer, Appl. Phys. Lett 74, 2516 (1999).
- [35] M. Hansen, Constitution of Binary Alloys (McGraw-Hill, New York, 1958).
- [36] Y. Park, J. Caballero, A. Cabbibo, and J. Childress, J. Appl. Phys. 81, 4717 (1997).
- [37] K. Kirk, J. Chapman, and C. Wilkinson, Appl. Phys. Lett. **71**, 539 (1994).
- [38] E. C. Stoner and E. Wohlfarth, Phil. Trans. Royal Soc. A250, 599 (1948).
- [39] C. Kittel, Phys. Rev. **70**, 965 (1946).
- [40] S. Chikazumi, *Physics of Magnetism* (John Wiley and Sons, New York, 1964).
- [41] E. Stoner, Phil. Mag. **36**, 803 (1945).
- [42] J. Osborn, Phys. Rev **67**, 351 (1945).

- [43] R. M. Bozorth, Ferromagnetism (D. Van Nostrand Company, New York, 1951).
- [44] Handbook of Microlithography, Micromachining, and Microfabrication, edited by P. Rai-Choudhury (SPIE Optical Engineering Press, Bellingham, Washington, 1997), Vol. 1: Microlithography.
- [45] J. E. Mahan, *Physical Vapor Deposition of Thin Films* (John Wiley and Sons, New York, 2000).
- [46] K. Kirk, J. Chapman, S. McVitie, P. Aitchison, and C. Wilkinson, Appl. Phys. Lett 75, 3683 (1999).
- [47] S.W.Yuan, H.N.Bertram, J. F. Smyth, and S. Schultz, IEEE Trans. Magn. 28, 3171 (1992).
- [48] M. Ruhrig, B. Khamsehpour, K. Kirk, J. Chapman, P. Aitchison, S. McVitie, and C. Wilkinson, Appl. Phys. Lett 75, 3683 (1999).
- [49] S. Chou, P. Krauss, and L. Kong, J. Appl. Phys. 79, 6101 (1996).
- [50] R. Meservey, P. Tedrow, and P. Fulde, Phys. Rev. Lett 25, 1270 (1970).
- [51] P. Tedrow and R. Meservey, Phys. Rev. Lett 26, 192 (1971).
- [52] M. Johnson, Phys. Rev. Lett 70, 2142 (1993).
- [53] M. Johnson, J. Appl. Phys. **75**, 6714 (1994).
- [54] A. Fert and S. Lee, J. Magn. Magn. Mat **165**, 115 (1997).
- [55] M. Johnson and R. Silsbee, Phys. Rev. B **35**, 4959 (1987).
- [56] M. Johnson and R. Silsbee, Phys. Rev. Lett. **60**, 377 (1988).
- [57] P. van Son, H. van Kempen, and P. Wyder, Phys. Rev. Lett. 58, 2271 (1987).
- [58] P. van Son, H. van Kempen, and P. Wyder, Phys. Rev. Lett. **60**, 378 (1988).
- [59] T. Valet and A. Fert, Phys. Rev. B 48, 7099 (1993).
- [60] M. Baibich, J. Broto, A. Fert, F. N. van Dau, F. Petroff, P. Etienne, G. Creuzet, A. Friedrich, and J. Chanzeles, Phys. Rev. Lett. 61, 2472 (1988).
- [61] G. Binach, P. Grunberg, F. Saurenbach, and W. Zinn, Phys. Rev. B 39, 4828 (1989).
- [62] S. F. Lee, W. P. Pratt, Jr. Q. Yang, P. Holody, R. Loloee, P. A. Schroeder, and J. Bass, J. Magn. Magn. Mater. 118, L1 (1993).
- [63] F. Jedema, A. Filip, and B. van Wees, Nature **410**, 345 (2001).

- [64] A. C. Reilly, W. Park, R. Slater, B. Ouaglal, R. Loloce, W. P. Pratt, Jr, and J. Bass, J. Magn. Magn. Mater. 195, L268 (1999).
- [65] A. B. Gougam, F. Pierre, H. Pothier, D. Esteve, and N. O. Birge, J. Low Temp. Phys 118, 447 (2000).
- [66] W. Pratt, S. Lee, J. Slaughter, R. Loloce, P. Schroeder, and J.Bass, Phys. Rev. Lett. 66, 3060 (1991).
- [67] S. Lee, W. Pratt, R. Loloee, P. Schroeder, and J.Bass, Phys. Rev. B 46, 548 (1992).

